Study of Solar Thermophotovoltaic (STPV) Energy Conversion with Selective Metafilm Coatings and GaSb Cell Separated by Glass Microspheres

by

Avinash Singh Nayal

A Thesis Presented in Partial Fulfillment
of the Requirements for the Degree
Master of Science

Approved July 2020 by the
Graduate Supervisory Committee:

Liping Wang, Chair
Robert Wang
Ryan Milcarek

ARIZONA STATE UNIVERSITY

August 2020

ABSTRACT

Solar energy as a limitless source of energy all around the globe has been difficult to harness. This is due to the low direct solar-electric conversion efficiency which has an upper limit set to the Shockley-Queisser limit. Solar thermophotovoltaics (STPV) is a much more efficient solar energy harvesting technology as it has the potential to overcome the Shockley-Queisser limit, by converting the broad-spectrum solar irradiation into a narrowband infrared spectrum radiation matched to the PV cell. Despite the potential to surpass the Shockley-Queisser limit, very few experimental results have reported high system-level efficiency.

The objective of the thesis is to study the STPV conversion performance with selective metafilm absorber and emitter paired with a commercial GaSb cell at different solar concentrations. Absorber and Emitter metafilm thickness was optimized and fabricated. The optical properties of fabricated metafilms showed good agreement with the theoretically determined properties. The experimental setup was completed and validated by measuring the heat transfer rate across the test setup and comparing it with theoretical calculations. A novel method for maintaining the gap between the emitter and PV cell was developed using glass microspheres. Theoretical calculations show that the use of the glass of microspheres introduces negligible conduction loss across the gap compared to the radiation heat transfer, which is confirmed by experimental heat transfer measurement. This research work will help enhance the fundamental understanding and the development of the high-efficiency solar thermophotovoltaic system.

ACKNOWLEDGMENTS

I would like to thank my thesis chair, Dr. Liping Wang, for giving me an opportunity to work under his supervision and carry out this research. I would like to thank my committee members Dr. Robert Wang and Dr. Ryan Milcarek for their timely support and guidance while revising this thesis. I would also like to thank Dr. Qing Ni and all other members of the Nano-Engineered Thermal Radiation Lab for their support and help during the thesis. I am also grateful to all my friends and family who supported me.

TABLE OF CONTENTS

LIST OF TABLES

LIST OF FIGURES

Figure Page

Figure Page

CHAPTER 1

INTRODUCTION

1.1 Background

The sun's radiation power falling on earth in 1 hour is greater than the power required by human society for an entire year. This energy was being first utilized by direct illumination of solar cells, but this direct utilization is very limited due to low energy conversion efficiency. This is due to the well-known Shockley-Queisser limit which is a theoretical upper limit for solar cells [1]. The broadband nature of the solar spectrum (ranging from approximately 200 nm to 2500 nm) is responsible for the low conversion efficiency. The incident photons with energy lower than the bandgap energy and higher than the bandgap energy result in the 30% upper limit for single-junction solar cells with no concentration, which is because the lower energy photons are not absorbed while the photons with extra energy lose the extra energy as heat. Solar thermophotovoltaics (STPV) could be an efficient solar energy conversion technology that has the potential to exceed the Shockley-Queisser limit [2]. This is achieved by absorbing the incident radiation in the entire solar spectrum and emitting the radiation in the narrowband infrared region to the photovoltaic cells.

STPV systems convert sunlight to electricity by absorbing photons as heat and emitting thermal radiation which is then converted into electron-hole pairs via a low energy bandgap PV cell. Figure 1 shows the STPV system in a simplified manner. Assume there is a perfect energy transmission from the absorber to the emitter. The interaction between the sun and the absorber (highlighted by blackbody radiation between the two components) is one part of the energy conversion process and the second part deals with the energy transfer between emitter and PV cell. There is an upper limit to the second part of the energy conversion which is governed by Carnot efficiency [3]. Here, the absorber/emitter is a blackbody receiving a net radiation heat flux from concentrated solar source. This makes the total efficiency η of the system becomes –

$$\eta = \left(1 - \frac{\varepsilon\sigma T^4}{\sigma {T_s}^4}\right) . \left(1 - \frac{T_c}{T}\right)$$

where T, T_s and T_c are the temperatures of the absorber/emitter, sun, and cell, respectively. A 70% system efficiency is achievable for an absorber/emitter temperature around 1000 K, which is nearly more than twice the Shockley-Queisser limit.

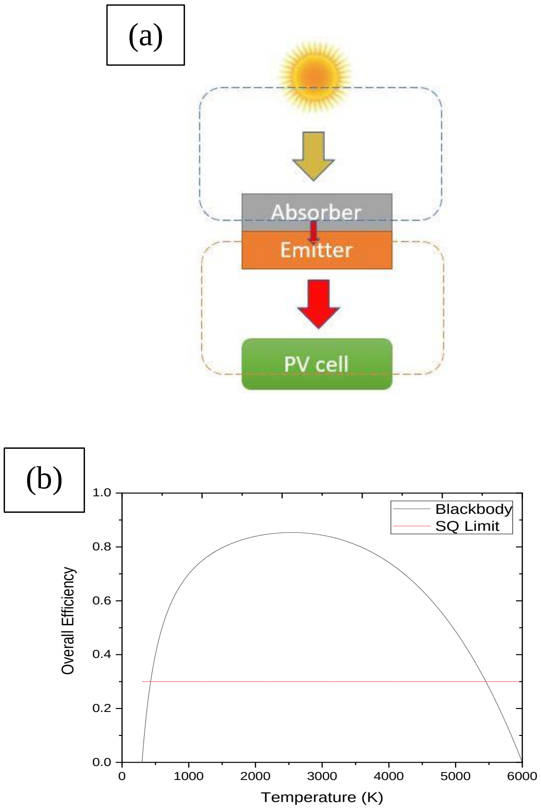

Figure 1.1 (a) Schematic of typical STPV configuration (b) Overall efficiency curve of an ideal STPV system, the sun and PV cells are modeled at 6000 K and 300 K blackbodies, respectively.

Higher the absorber/emitter temperature, higher is efficiency but in practice, it is very hard to reach high temperatures such as the temperature of maximum efficiency i.e. 2544 K as shown in Figure 1.1(b). This is due to huge heat losses from conduction, convection, and radiation of air, as well as conduction losses from the sample holder. This induces huge parasitic losses from absorber and emitter, resulting in a lower operating temperature of the system. Despite requiring high operating temperatures for high efficiency, the PV cell needs to be kept cool for better performance, as the power and efficiency of the cell decrease with a rise in temperature (0.4%-0.5% per K for silicon solar cells) [4]. There's also the matter of oxidization of optically qualified materials at high operating temperatures, leading to the requirement of a vacuum environment. Absorber, emitter, and PV cell temperatures are controlled to ensure they operate in their best conditions to perform efficiently. Moreover, efficient radiation transfer is also required for high system efficiency, also the absorber is supposed to exchange photons only with the sun [4]. This implies that a high concentration of sunlight is required (which is essential for high absorber/emitter temperature). Also, the emission spectrum of the emitter must be narrowband, and the emission peak must match the bandgap of the PV cell, as implied by the Carnot term in the efficiency equation.

In conclusion, two vital components will lead to a satisfactory STPV system performance. First is the temperature control of the absorber/emitter/PV cell system as the sun to absorber efficiency decreases with increasing absorber temperature. The same is the case with PV cells, its power and efficiency decrease with increasing temperature. A possible solution to this problem is the use of an optical filter like an IR-shield and spectral filter above the absorber and between emitter and cell to recycle the photons respectively.

There are numerous methods of cooling solar cells such as phase change materials based on photovoltaic applications. A novel concept of changing the spectral response of the solar cells to electromagnetic waves for the passive cooling of the cells has been developed in recent years [5]. The second vital component for an adequate STPV performance is efficient radiation transportation [2]. The efficient energy transportation can be achieved by successfully integrating three key aspects: high solar concentration, radiation losses from emitter due to limited view factor, and narrowband emission of the emitter to surpass the Shockley-Queisser limit.

The desirable behavior of absorber to absorb maximum solar radiation and minimize the thermal radiation emitted in the infrared region is known as spectral selectivity. This behavior is crucial in increasing the STPV system efficiency. For example, a spectrally selective emitter is usually utilized as the TPV cells react only to a narrow wavelength range i.e. near bandgap energy, the emission from the emitter must match the spectral response of the cells. Similarly, a spectrally selective absorber should have high absorption in the visible range and low emission in the infrared region. But the performance of these spectrally selective absorbers not only depends on their absorption and emission behavior but also on the bandwidth of the transition region between high absorption and low emission.

1.2 Literature Study

Recently the focus has been on the main three components of an STPV system, i.e. absorber, emitter, and the PV cell, to increase the overall system performance. Spectrally selective absorbers have been explored [6][7][8] to suppress the self-radiation losses from the absorber to improve the energy conversion efficiency. Under low concentrations, selective absorbers are more useful as their self-radiation is comparable with solar energy and as there are usually high solar concentrations in STPV systems, the benefit gained from employing a selective absorber is small [2].

The thermal transfer efficiency (η_a) as a function of solar concentration and temperature of the absorber was calculated for both blackbody absorbers and selective absorbers by Wang et al [9].

$$\eta_a = \frac{C \int \alpha(\lambda) E_{solar}(\lambda) d\lambda - \int \alpha(\lambda) E_B(\lambda, T) d\lambda}{C \int E_{solar}(\lambda) d\lambda}$$

They found that selective absorbers were able to suppress the radiation loss efficiently in the low concentration-high operating temperature regime, whereas the blackbody absorber performs better in a high concentration-low operating temperature regime. Given the best-operating conditions, both the absorbers may yield similar thermal transfer efficiency, which was experimentally proven by Lenert et al.[10] and Rinnerbauer et al.[11]. The selective absorber is more advantageous as it requires lower solar energy input for the same absorber temperature as compared to a blackbody absorber.

The performance of selective absorber depends also on the bandwidth of transition region between the high absorption and low emission band, as the energy losses due to spectral overlap between concentrated solar and radiation spectrum become significant at elevated operating temperatures. A ~20% efficiency drop was observed when the transition bandwidth increases from 0 to 2 µm[9]. Therefore, a sharp cut-off is required for high-temperature solar absorbers. Multitudes of designs have been discussed for blackbody and solar absorber in the past decade and only a handful of them have been able to contribute to a high-performance STPV system.

Some of the absorber designs are also incorporated in thermal emitters by slightly changing their structural parameters. This is possible as Kirchhoff's law of thermal radiation states the equivalency of absorptivity and emissivity. Edge emitters (absorptivity with a step-function) and narrowband emitters (absorptivity with a narrow band) have currently emerged as the two major categories in thermal emitters in the field of STPV. The choice between them is usually dependent on the internal quantum efficiency (IQE) of the PV cell. This is because the emission spectrum should match the high IQE part of the cell to achieve high emitter to cell efficiency. Edge emitters are used in most of the STPV experiments since using narrow-band emitters leads to a large decrease in power density, whereas the gain in efficiency is not high enough to compensate. Bauer [12] introduced sub-bandgap and above-bandgap suppression coefficients into his model to study the effect of emission bandwidth. The results indicated that both above and sub-bandgap suppression can enhance the system efficiency, with sub-bandgap suppression having more effect than the latter.

In the actual experimental setup, it is hard to reach unity in absorptivity for both absorber and emitter at target wavelength which is required for high system efficiency. Lenert et al.[13] tried to bridge this gap between theoretical predictions and experimental results as they discussed the role of possible spectral non-idealities of absorbers and emitters. The current emitters in use are still very far from ideal emitters either in optical performance or thermal stability. The most challenging aspect of this is fabricating a robust emitter on the hot side of the system due to the constraints of thermal stability. One possible solution is to improve the emission spectrum on the cold side of the system i.e. the PV cell. This can be achieved by using an optical filter adhering to the cell, which will help in suppressing the sub-bandgap photons. Bierman et al. [14] were able to increase their system efficiency from 3.2% to 6.8% through the addition of a tandem plasma-interference filter in the STPV setup. However, their filter still deviates from a perfect narrowband emitter as it aims only on suppressing emissions below the bandgap energy. Another way to incorporating the spectrally selective solar absorber and the thermal emitter is a multilayer structure, which is based on the anti-reflection effect or cavity resonance [15][16][17]. An STPV system with a multilayer based solar absorber and thermal emitter was developed by Shimizu et.al[18]. They recorded a total system efficiency of 8% with the absorber/emitter at a temperature of 1640 K.

As per the current systems, lower bandgap PV cells are used by the low-temperature emitters. Mostly, III-V semiconductors are used for this purpose such as GaSb (0.7 eV)[19][20][21], InGaAs (0.6 – 0.7 eV)[22][23][24], and InGaAsSb (0.5 – 0.6 eV) [10], which all demonstrated high light to electricity conversion efficiency. Usually, other cells have inappropriate bandgaps which often leads to disappointing outputs. For example, InGaAsSb PV cells have bandgap between 0.35 and 0.5 eV but also have low open-circuit voltage which decreases its overall efficiency [25]. Generally, three factors are used to characterize the efficiency of PV cells. These are the ultimate efficiency, the voltage factor, and the fill factor. The efficiency model for a real solar cell differs from Shockley's model which was first introduced by Shockley and Queisser in their detailed balanced model of solar cells [1][26]. According to Shockley's model photons with energy greater than the bandgap energy contributes to the electric power output, but it comes with an added complication. The higher energy photons result in thermalization losses from cell i.e. there will be energy loss due to the difference between incoming photon energy and cell bandgap which causes heating due to thermalization. The real cell also differs from Shockley's model in another key aspect i.e. input radiation which is supposed to be the thermal emission of the emitter and not the solar spectrum.

Emitter temperature usually decides the upper limit of the cell efficiency. Moreover, high power density is achieved when the emitter temperature is high enough that the blackbody emission spectrum peak matches the bandgap. The peak is dependent on the mathematical form of Planck's law. The peak of solar spectrum shifts from visible region to near-infrared when plotted in frequency units compared to wavelength units [27]. The density distribution function is used to describe radiation in terms of wavelength or frequency. After further rumination of the calculation of cell, efficiency leads to a conclusion that neither method is precise for peak calculation. Instead, the density distribution of photon numbers is a better alternative as it gives a clear physical interpretation [2]. System efficiency can be theoretically increased without the spectrum peak matching the bandgap of the cell, as high-only high-power density is achieved through this matching. However, in practice, there are many benefits of high-power density like, reduction in parasitic losses which thereby increases the system efficiency.

1.3 Objectives

The main objective of the thesis is to experimentally study the STPV conversion performance with selective metafilm absorber and emitter paired with a commercial GaSb cell at different solar concentrations. Chapter 2 presents the theoretical methods used to predict the thermal and electrical performance of the STPV systems which are used in chapter 4 to validate the experimental setup by calculating the side losses and conduction losses and the theoretical calculations for efficiency to check the improvement in the performance of the system. Chapter 3 describes one of the major challenges is to create microscale vacuum gaps between the absorber-emitter module and the PV cell with minimized energy losses, and this is achieved by using SiO_2 microbeads as spacers. It also contains demonstrates how to deposit the absorber and emitter metafilm layer on the SS substrate to develop the absorber emitter module. It also reports the experimental results and compares them with the theoretical calculations. Finally, Chapter 4 discusses the conclusion and future work. Then experiments were performed using the solar simulator in Dr. Liping Wang’s lab.

CHAPTER 2

THEORETICAL METHODS FOR MODELLING STPV SYSTEMS

2.1 Radiation Heat Transfer Model of the STPV System

A comprehensive thermodynamic model was developed to evaluate the flow of power throughout the STPV system. For a known value of incident irradiation (Q_{in}), the emitter temperature at thermal equilibrium can be evaluated by solving the subsequent equation.

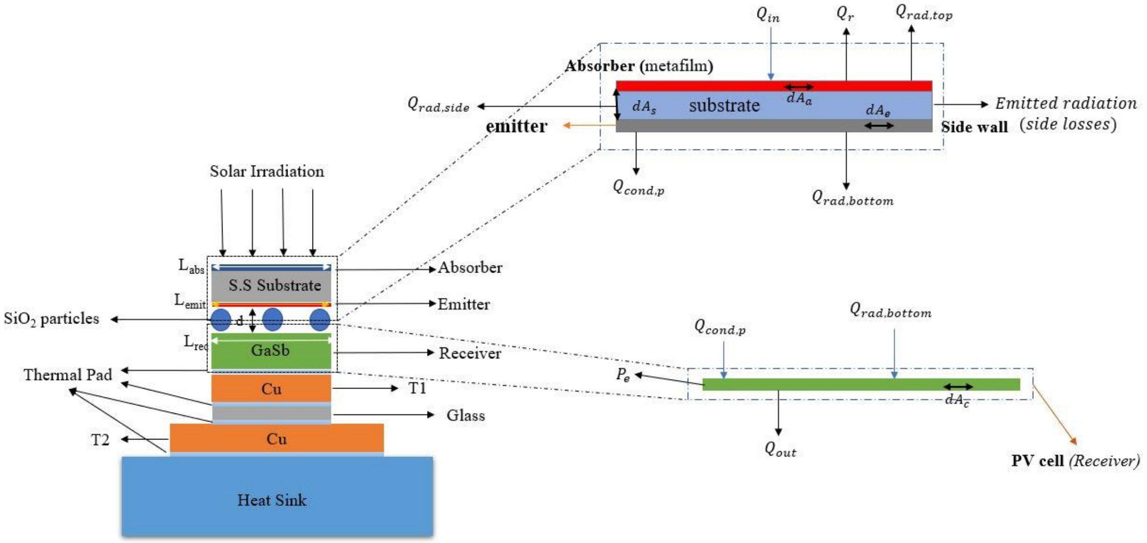

Figure 2.1: Schematic of the planar STPV system

$$Q_{in} - Q_r - Q_{rad,top}(T) - Q_{rad,side}(T) = Q_{rad,bottom}(T) + Q_{cond,p}(T) \qquad \textbf{(1)}$$

Here, Q_{in} is the normally incident solar radiation on the absorber's surface. Whereas, Q_r is the measure of incident power reflected off the absorber's surface. $Q_{rad,top}(T)$ is the thermally radiate power lost from the absorber surface and is defined using Planck's blackbody equation and measured spectral emissivity of the absorber surface. $Q_{rad,side}$ is the loss in power due to radiation from the four sides of the tungsten sputtered substrate and is calculated using the emissivity of the substrate. For simplicity of calculations, it has been assumed that $T_{abs} = T_{subs} = T_{emit}$. On the R.H.S of equation (1), $Q_{cond,p}(T)$ represents the power loss due to conduction from the silica particles.

$$Q_{in} = \int_{A_a} \int_0^\infty G_{AM1.5}(\lambda) C d\lambda \, dA_a \tag{2}$$

$$Q_r = \int_{A_a} \int_0^\infty \{1 - \alpha_a(\lambda)\} H(\lambda) d\lambda dA_a \tag{3}$$

$$Q_{rad,top} = \int_{A_a} \int_0^\infty \varepsilon_a(\lambda) \{E_b(\lambda, T_{abs}) - E_b(\lambda, T_{envir})\} d\lambda dA_a \tag{4}$$

$$Q_{rad,side} = \int_{A_s} \int_0^\infty \varepsilon_s(\lambda) \{E_b(\lambda, T_{subs}) - E_b(\lambda, T_{envir})\} d\lambda \, dA_s \tag{5}$$

$$Q_{rad,bottom} = \int_{A_e} \int_0^\infty \frac{E_{b\lambda}(T_{emit}) - E_{b\lambda}(T_{cell})}{\frac{1 - \varepsilon_{emit}(\lambda)}{\varepsilon_{emit}(\lambda)} + \frac{1}{F_{emit-cell}} + \frac{1 - \varepsilon_{cell}(\lambda)}{\varepsilon_{cell}(\lambda)}} d\lambda \, dA_e \tag{6}$$

$$Q_{cond,p} = \frac{T_e - T_c}{R_{cond}} \tag{7}$$

$$E_b(\lambda, T) = \frac{2\pi h c^2}{\lambda^5 [e^{hc/\lambda k_B T} - 1]} \tag{8}$$

Lastly, $Q_{rad,bottom}(T)$ is the net power emitted from the surface of the emitter due to radiation and is computed in a similar way using Planck's blackbody equation and measured spectral emissivity of the emitter surface. The whole STPV setup was installed inside a vacuum chamber to minimize convections losses. Hence, they are ignored for simplicity of calculations. In the calculations, the emissivity of the involved surfaces is simply assumed to be (1-Reflectivity).

In the aforementioned equations, $G_{AM1.5}(\lambda)$ is the solar spectrum at AM1.5 global tilt (Air Mass 1.5 Spectra) and C is the optical concentration factor. Blackbody spectral emissive power is given by $E_b(\lambda, T)$. Spectral absorptance of the absorber is given by $\alpha_a(\lambda)$.Whereas, the spectral emissivity of the absorber, emitter, substrate, and cell are given respectively by, $\varepsilon_a(\lambda)$, $\varepsilon_{emit}(\lambda)$, $\varepsilon_s(\lambda)$ and $\varepsilon_{cell}(\lambda)$. Spectral absorptivity is equal to spectral emissivity for all surfaces as per Kirchhoff's law. Radiative view factor between emitter and TPV cell denoted as $F_{emit-cell}$, and was computed as 0.98. This implies that approximately 2% of the energy radiated by the emitter is not captured by the cells. This energy loss is also referred to as cavity loss. Emitter and TPV cell temperatures were represented by T_e and T_c respectively, whereas $R_{cond,p}$ denoted the thermal resistance of the particles.

2.2 Estimation of Conduction Heat Transfer via Glass Microspheres

The conduction losses from the support were evaluated using the Hertz's Model. The thermal resistance of the SiO_2 particles is computed using the equations 8-13. Here, S is the distance between emitter and cell, which in this case is equal to the diameter of the SiO_2 particles. The effective contact area of the SiO_2 particles is represented by A. N is the total number of particles in contact, i.e. 5 in our case. F denotes the weight on the particles, which is the weight of the absorber-emitter module. Young's modulus and poison's ratio of glass microspheres and cell are represented by E_{SiO2},E_c,v_{SiO2} and v_c, respectively. The radius of curvature is expressed by R.

$$R_{cond,p} = \frac{S}{k_{SiO_2} \times A} \tag{9}$$

$$A = N \times (\pi a^2) \tag{10}$$

$$a = \left(\frac{3PR}{4E}\right)^{\frac{1}{3}} \quad \textbf{(11)}$$

$$P = \frac{\mathrm{F}}{N} \quad \textbf{(12)}$$

$$\frac{1}{E} = \frac{1-\nu_{SiO2}^2}{E_{SiO2}} + \frac{1-\nu_c^2}{E_c} \quad \textbf{(13)}$$

$$\frac{1}{R} = \frac{1}{R_1} + \frac{1}{R_2} \quad \textbf{(14)}$$

2.3 Electrical Model of the STPV System

The overall system efficiency of the STPV system is the ratio of electrical output power from the cell P_e to the incident solar heat flux q_{in} and is defined as

$$\eta_{STPV} = \frac{J_{SC}V_{OC}FF}{q_{in}} \quad \textbf{(15)}$$

Where J_{SC} (A/cm^2) is the short-circuit current density of the cell and is calculated as –

$$J_{SC} = \int_0^{\frac{hc_0}{E_g}} \frac{e\lambda}{hc_0}\eta_{IQE,\lambda}q_{rad,bottom,\lambda}d\lambda \text{ [32]} \quad \textbf{(16)}$$

Here, E_g is the bandgap of the GaSb TPV cell, e is the elementary charge and $\eta_{IQE,\lambda}$ is the internal quantum efficiency (IQE) of the cell. The open-circuit voltage (V_{OC}) is computed as

$$V_{OC} = \left({k_BT_C}/{e}\right) ln\left({J_{SC}}/{J_0}+1\right) \text{ [32]} \quad \textbf{(17)}$$

Where J_0 is the dark current and is evaluated using the following equation –

$$J_0 = e.\left(\frac{n_i^2D_h}{L_hN_D} + \frac{n_i^2D_e}{L_eN_A}\right) \quad \textbf{(18)}$$

Here, n_i is the intrinsic carrier concentration of the cell, D_h and D_e represent the diffusion coefficient for hole and electron respectively. L_h and L_e are the hole and electron diffusion length respectively, whereas N_D and N_A are the donor and acceptor concentration respectively. The fill factor for the cell is calculated using the equation given by Park et al.[32]

$$FF = \left(1 - \frac{1}{y}\right)\left(1 - \frac{\ln y}{y}\right) \qquad \textbf{(19)}$$

$$y = \ln\left({}^{J_{SC}}/_{J_0}\right) \qquad \textbf{(20)}$$

The absorptance, IQE, and parameters of the TPV cell used to calculate J_0 were taken from [33] and are mentioned in table 3.1. In this work the TPV cell studied is GaSb with a bandgap of 0.72 eV [34].

Basic Parameters	Numerical Value
Intrinsic carrier concentration n_i, at 300 K	1.405×10^{12} cm^{-3}
n-type dopant concentration, N_D	1.5×10^{18} cm^{-3}
p-type dopant concentration, NA	1.5×10^{19} cm^{-3}
Hole Lifetime, τ_h	8.7 ns
Electron Lifetime, τ_e	0.4 ns
Hole Diffusion length, L_h	4.44 µm
Electron Diffusion length, Le	2.42 µm

Table 2.1: Basic Parameters of GaSb cell

Hole and Electron diffusion coefficient were calculated using the relation –

$$L_e = \sqrt{D_e \tau_e} \ \& \ L_h = \sqrt{D_h \tau_h} \qquad \textbf{(21)}$$

The detailed calculations for calculating the hole/electron diffusion lengths and diffusivity can be found in Ref [34].

2.4 Predicted Thermal and Electrical Performance

The thermal and electrical performance of the STPV system was evaluated according to the theoretical methods described in the above sections. Fig. 2.2 shows the Radiation heat flux, conductions losses from the SiO_2 spacers, and the absorber temperature plots at varying concentration factors for three different receivers. Here, radiation heat flux is defined as the radiation emitted from the emitter towards the TPV cell i.e. $\frac{Q_{rad,bottom}}{A_e}$. Doped-Si, Black surface, and GaSb cell were used as the three receivers, and their optical properties used in the calculations were measured using the integration sphere as mentioned in chapter 3. We can see that for the case with GaSb cell the absorber temperature, which is the same as emitter temperature as per our assumption, is higher compared to the other two receivers. The same is the case of the conduction losses, but the magnitude of conduction losses are nominal compared to the other energy losses. Whereas the radiation heat flux of the GaSb cell is lowest among the three receivers since the GaSb cell has very low absorptance in the visible and near-IR range as compared to the other two receivers.

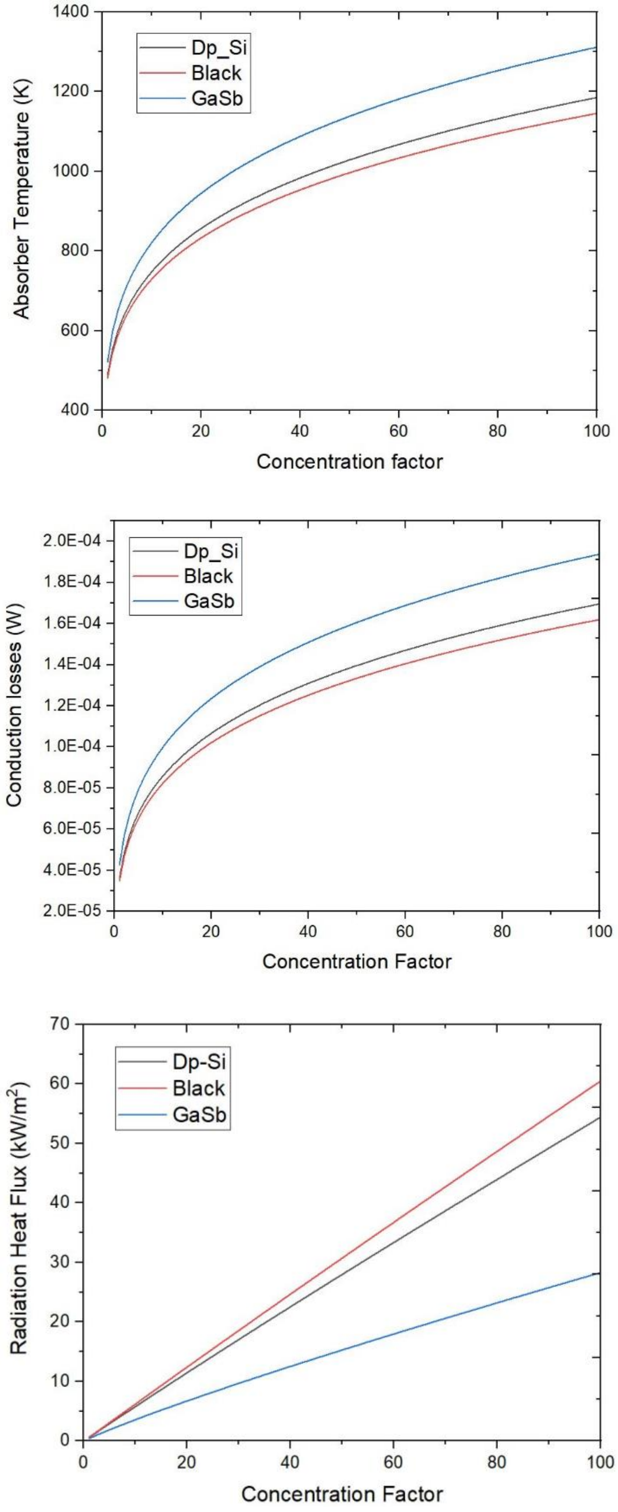

Figure 2.2: (Top) Absorber Temperature (Middle) Conduction Losses (Bottom) Radiation Heat Flux plots at varying concentration factors for three different receivers with fabricated absorber/emitter metafilm

An energy pie chart is used to present the major contributing factors in the heat transfer process starting from the radiation absorption from the absorber surface to the emitted radiation from the emitter to the receiver. This energy analysis is computed for Dp-Si, Black Surface, and the GaSb cell as receivers at concentration factors of 1, 20, 40, and 60 suns. Absorber temperature is mentioned for each concentration factor. From the energy pie-chart, we can see that conduction loss from the SiO_2 supporters are negligible whereas the side losses from the tungsten sputtered substrate and reflection losses from the absorber surface are also low. Emission from the absorber surface is the major energy loss for each of the three receivers and this energy loss increases with increasing concentration factors.

Dp_Si

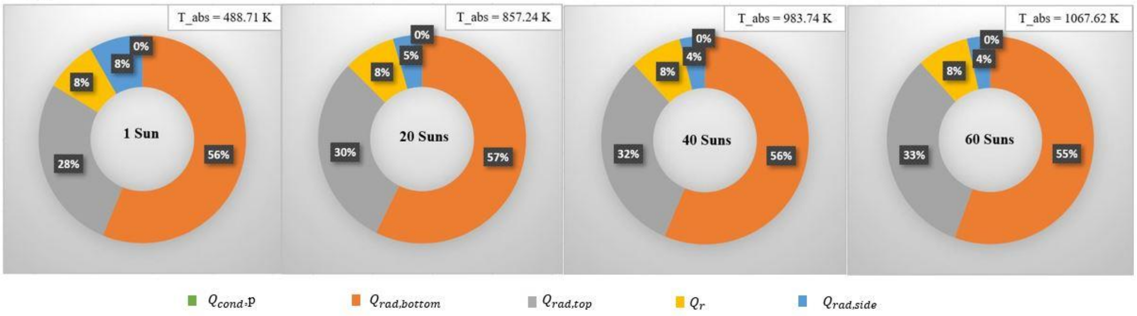

Black Surface

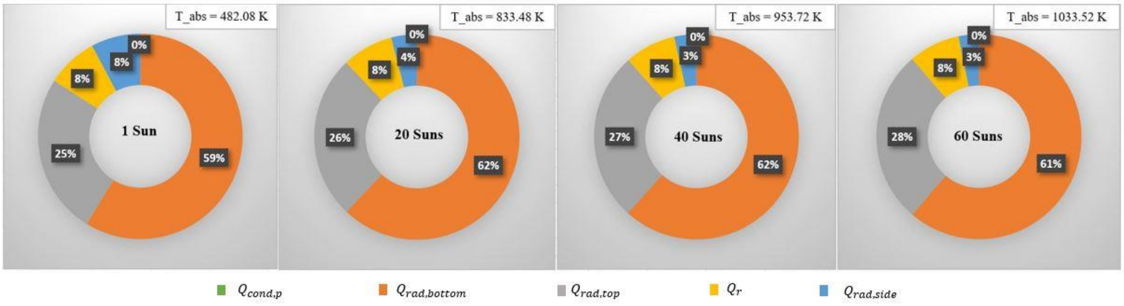

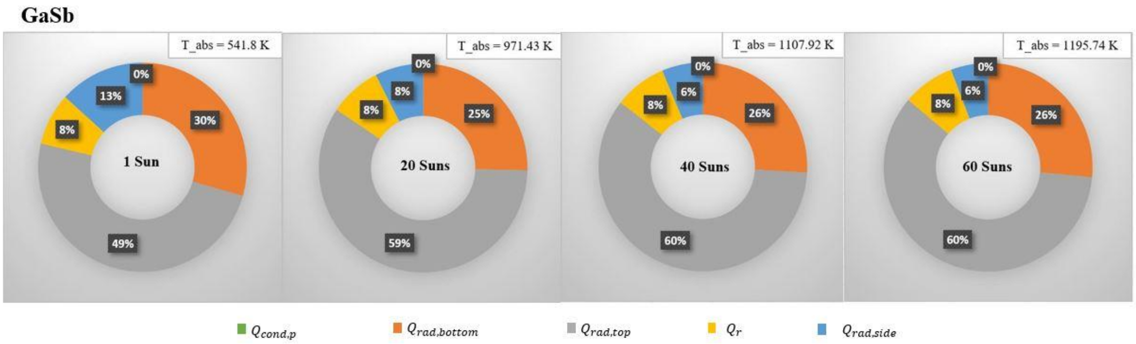

Figure 2.3: Energy Pie-chart for (Top) Dp-Si, (Middle) Black Surface, and (Bottom) GaSb cell as receivers and fabricated absorber/emitter metafilm

STPV system efficiency was evaluated for the GaSb cell as described in section 2.3. The measured optical and electrical properties of the GaSb cell were used in computing the overall efficiency of the system.

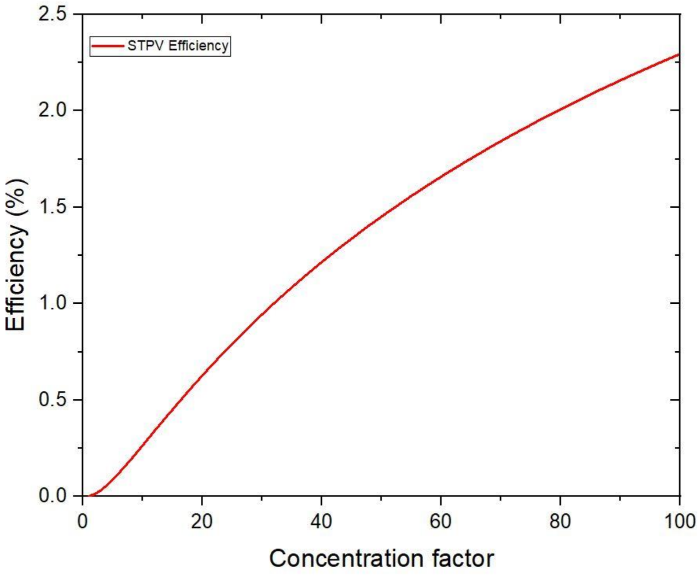

Figure 2.4: Predicted STPV Efficiency for GaSb cell with fabricated absorber/emitter metafilm

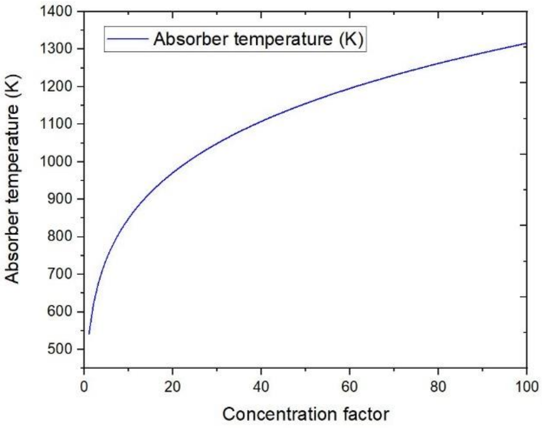

Figure 2.5: Predicted Absorber/Emitter temperature

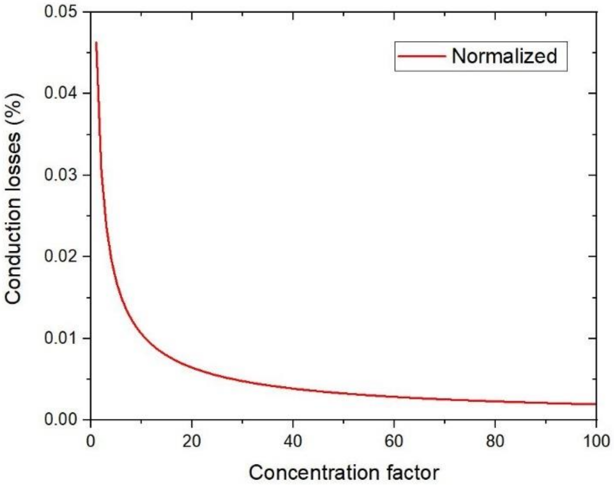

Figure 2.6: Predicted Conduction losses from the SiO_2 spacers

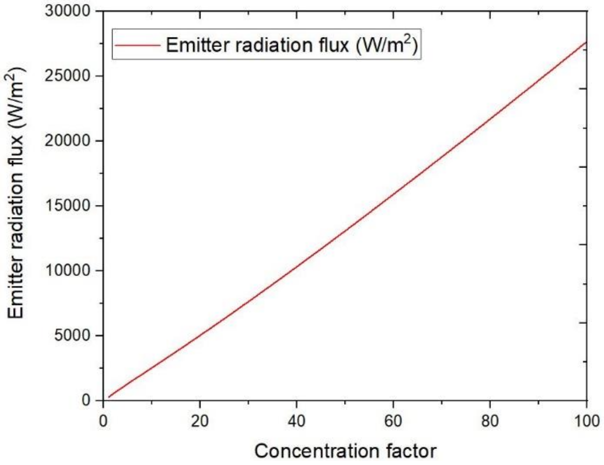

Figure 2.7: Predicted radiation heat flux from emitter to cell

The conduction losses in Fig. 2.6 are normalized with respect to incident solar power.

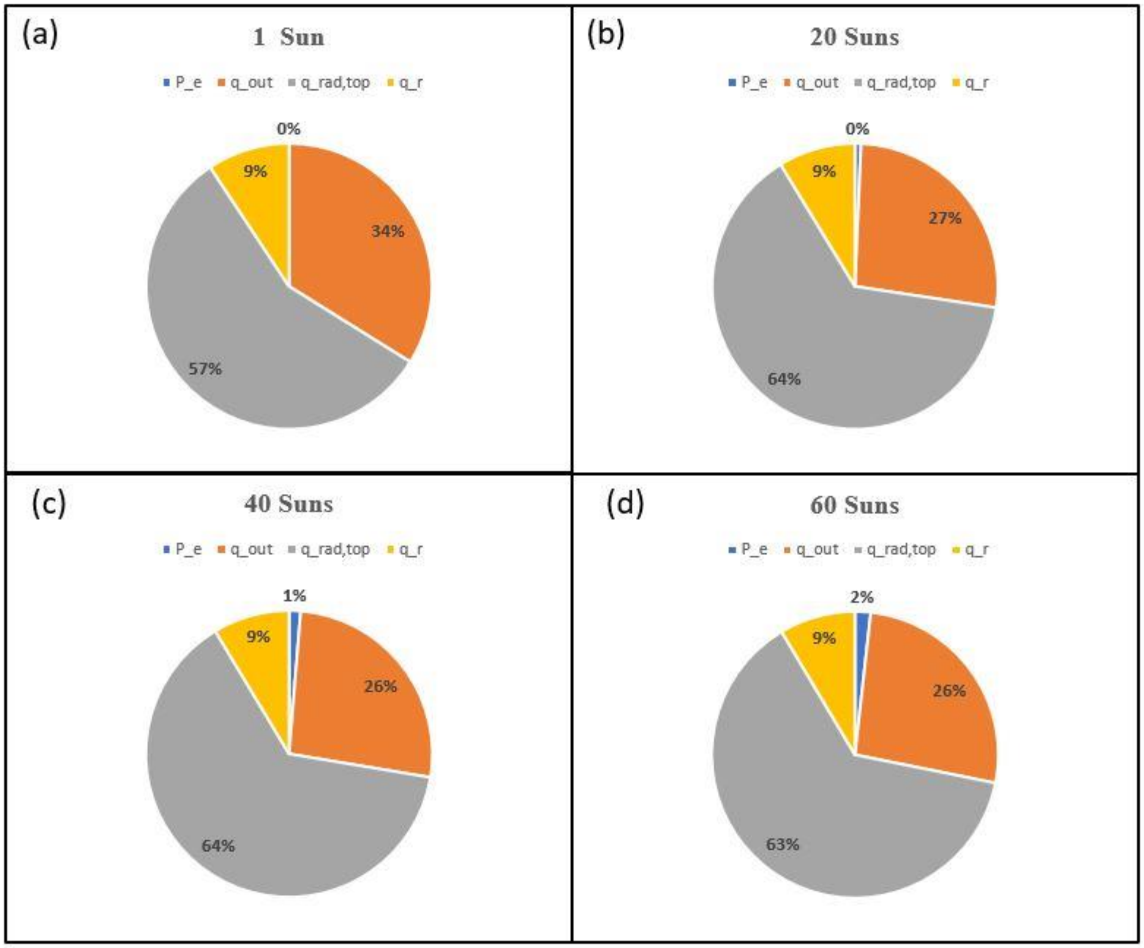

Figure 2.8: Energy pie-chart of the STPV system at (a) 1 Sun (b) 20 Suns (c) 40 Suns (d) 60 Suns.

2.5 Ideal Selective Filter

According to the energy loss analysis mentioned above, thermal emissions from the top surface of the absorber is the main contributing factor for low STPV performance. One feasible alternative to increase the efficiency of the STPV system by reducing this thermal emission loss is the use of an ideal selective reflector/emitter. The selective filter/reflector allows the incoming visible - near IR (cut-off) wavelength light to irradiate over the absorber surface. While it blocks the light above the cut-off wavelength and thereby, promoting photon recycling and reducing the thermal emission losses.

Here, we consider an ideal selective filter/reflector with a diffuse reflective surface above the solar absorber to recycle the thermal emission from the absorber surface as shown in figure 2.9. It’s is assumed to have the same temperature as the environment (300K), thus there is no radiation exchange between the filter and environment. The selective filter/reflector is considered close enough to the absorber surface to maintain a view factor of 1 maximizing the radiation exchange between the absorber and filter. Figure 3.20 shows the ideal behavior of the selective filter/reflector.

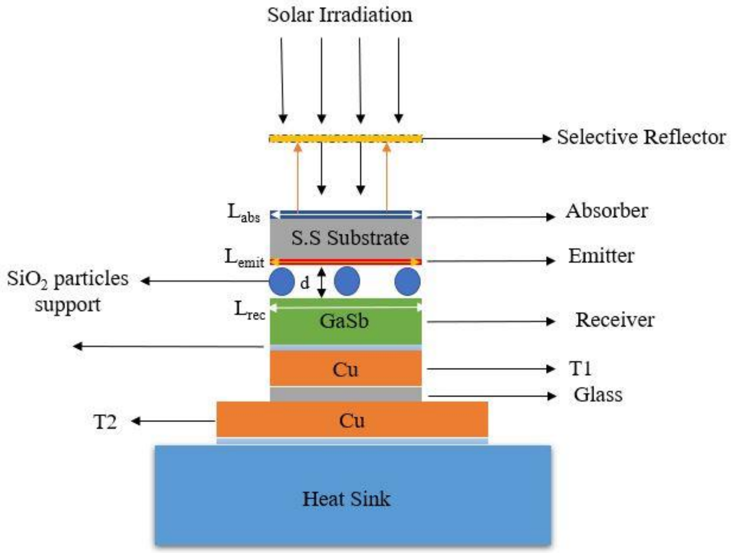

Figure 2.9: Schematic of the STPV system with ideal selective filter

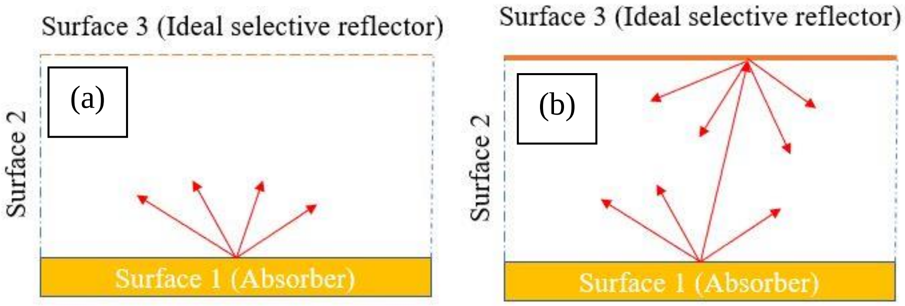

Figure 2.10: Ideal selective filter behavior (a) below cut off wavelength (b) above cut off wavelength

Equations for thermal emission loss from the top of the absorber surface for both the cases (i.e. below cutoff wavelength and above cutoff wavelength which is 2 µm in our case) –

$$\lambda \leq 2\mu m \qquad q_{rad,top} = \int_{0.4\mu m}^{2\mu m} \varepsilon_1(\lambda) \times \left(E_{b\lambda}(T_{abs}) - E_{b\lambda}(T_{envir})\right) d\lambda \qquad \textbf{(22)}$$

$$\lambda > 2\mu m \qquad q_{rad,top} = \int_{2.1\mu m}^{14\mu m} \frac{E_{b\lambda}(T_{abs}) - E_{b\lambda}(T_{envir})}{\frac{1}{F_{13}} + \frac{1-\varepsilon_3}{\varepsilon_3} + \frac{1-\varepsilon_1(\lambda)}{\varepsilon_1(\lambda)}} d\lambda \qquad \textbf{(23)}$$

Here, $F_{13} = 1$, which is the view factor between absorber top surface and selective filter. For the case of below cut off wavelength transmission from the filter is 100 % i.e. $\tau_3 = 1$ and for the case above cut off wavelength reflectivity of the filter is 100 % i.e. $\rho_3 = 1$ and $\alpha_3 = \varepsilon_3 = 0$. Energy analysis for three different absorbers (i.e. fabricated metafilm, Black absorber, ideal absorber) with and without the selective filter was computed. Figures 2.11, 2.12, and 2.13 show the energy pie-chart for the three different absorbers at different concentration factors. Figures 2.14 and 2.15 show the absorber temperature and STPV efficiency respectively for the different absorbers for the cases of with and without a filter.

The energy pie-charts show that with the inclusion of ideal selective filter/reflector emission losses from the absorber's top surface will reduce and concurrently the electrical power produced from the PV cell will increase for both the metafilm absorber and black absorber. Whereas, for the case of ideal absorber with filter the power produced approximately remains the same as in the case of without filter. This is due to the spectrally selective absorber whose cut-off wavelength is near to the cut-off wavelength of the filter. The reduction in emission losses from the absorber surface and recycled photons result in higher absorber temperature for both metafilm and black absorber as shown in Fig. 2.14. For the case of an ideal absorber, the performance of the system remains the same for with and without the filter, as its cut-off wavelength is less than the cut-off wavelength of the filter. This results in higher power exchange between the emitter and PV cell and thus increase in thermalization losses.

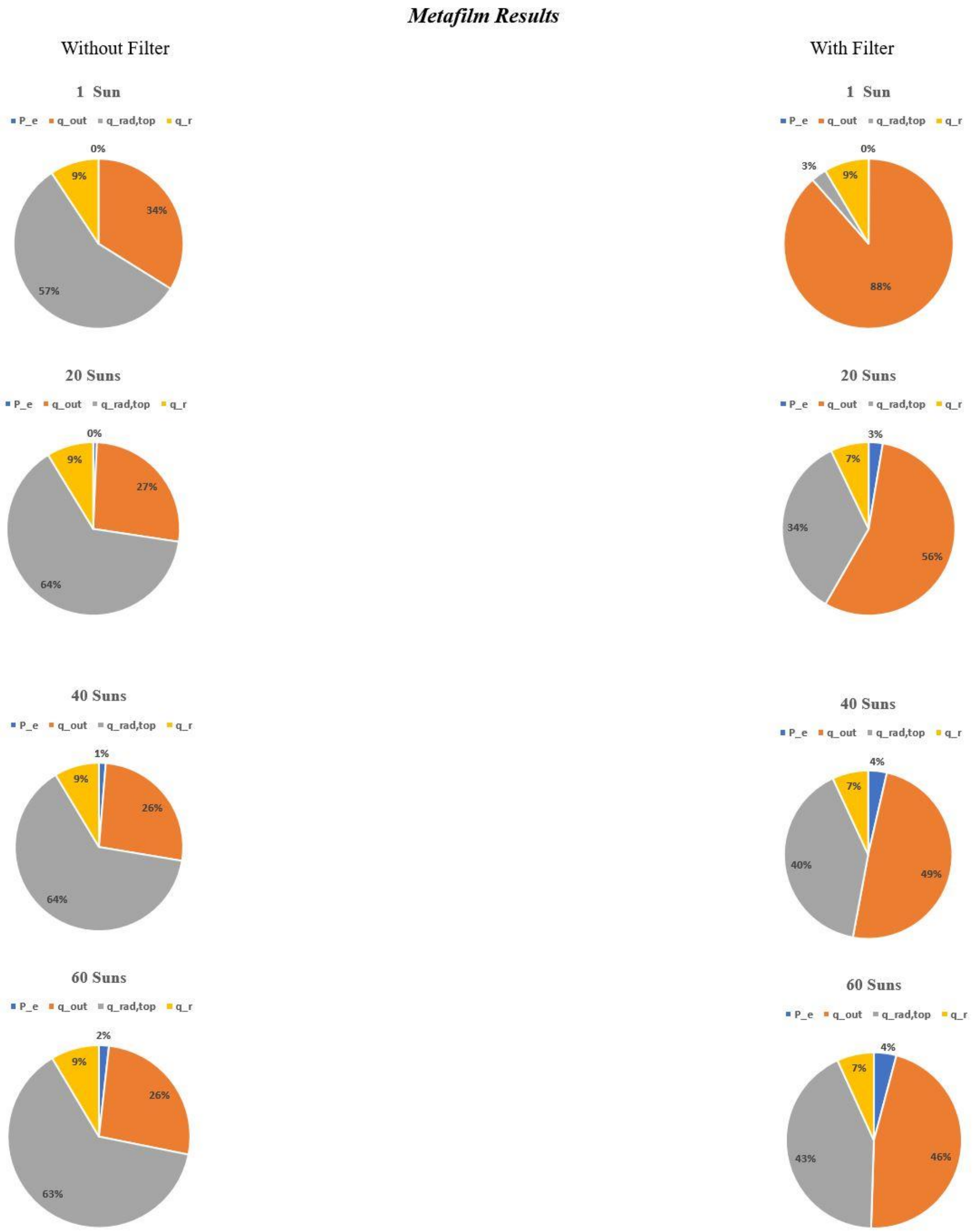

Figure 2.11: Energy Pie-chart for the fabricated metafilm absorber

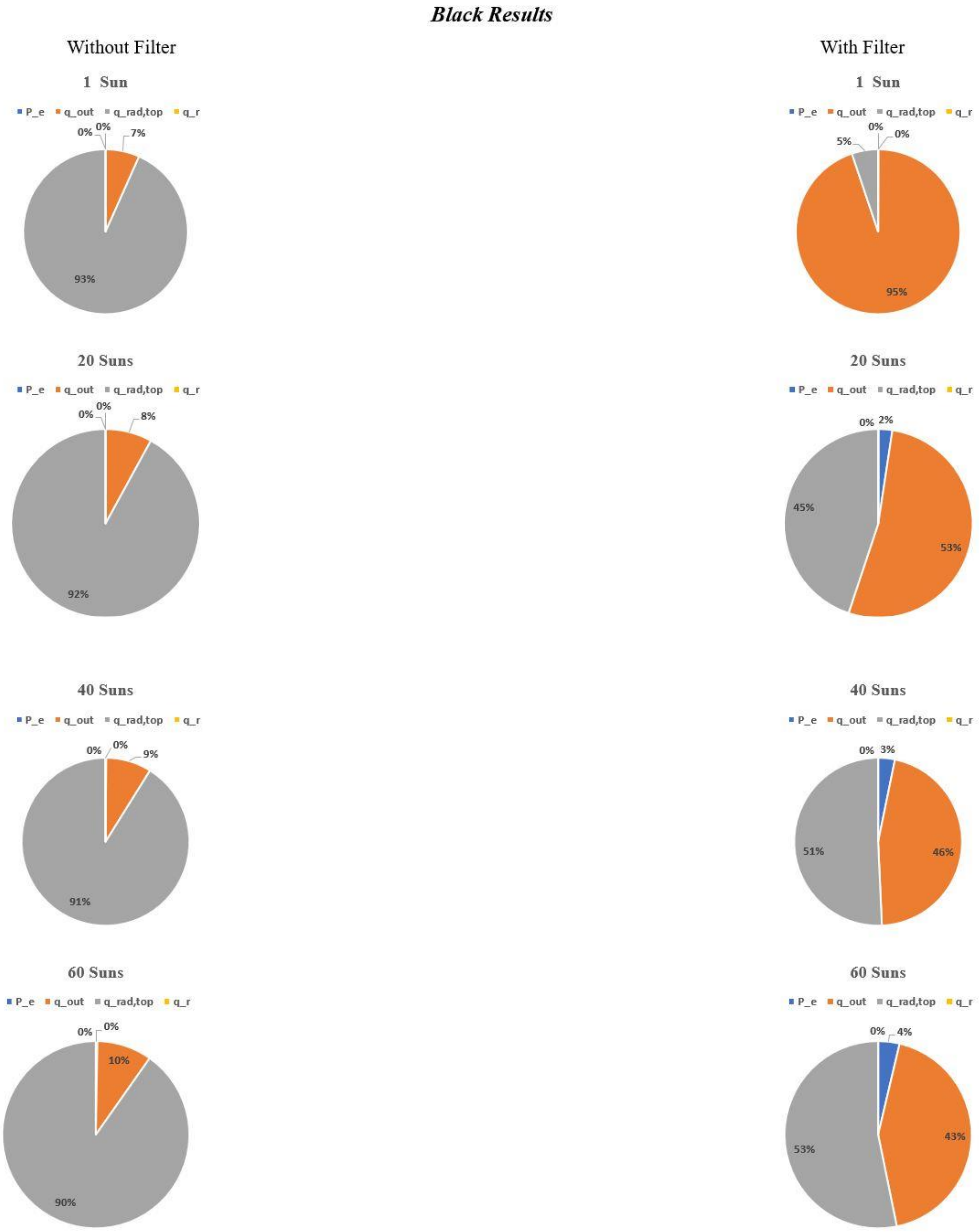

Figure 2.12: Energy pie-chart for black absorber

The ideal absorber has a 100 % absorption up to cut-off wavelength and 0 % absorption above the cut-off wavelength. The cut off wavelength for the ideal absorber was taken as 1.7 µm.

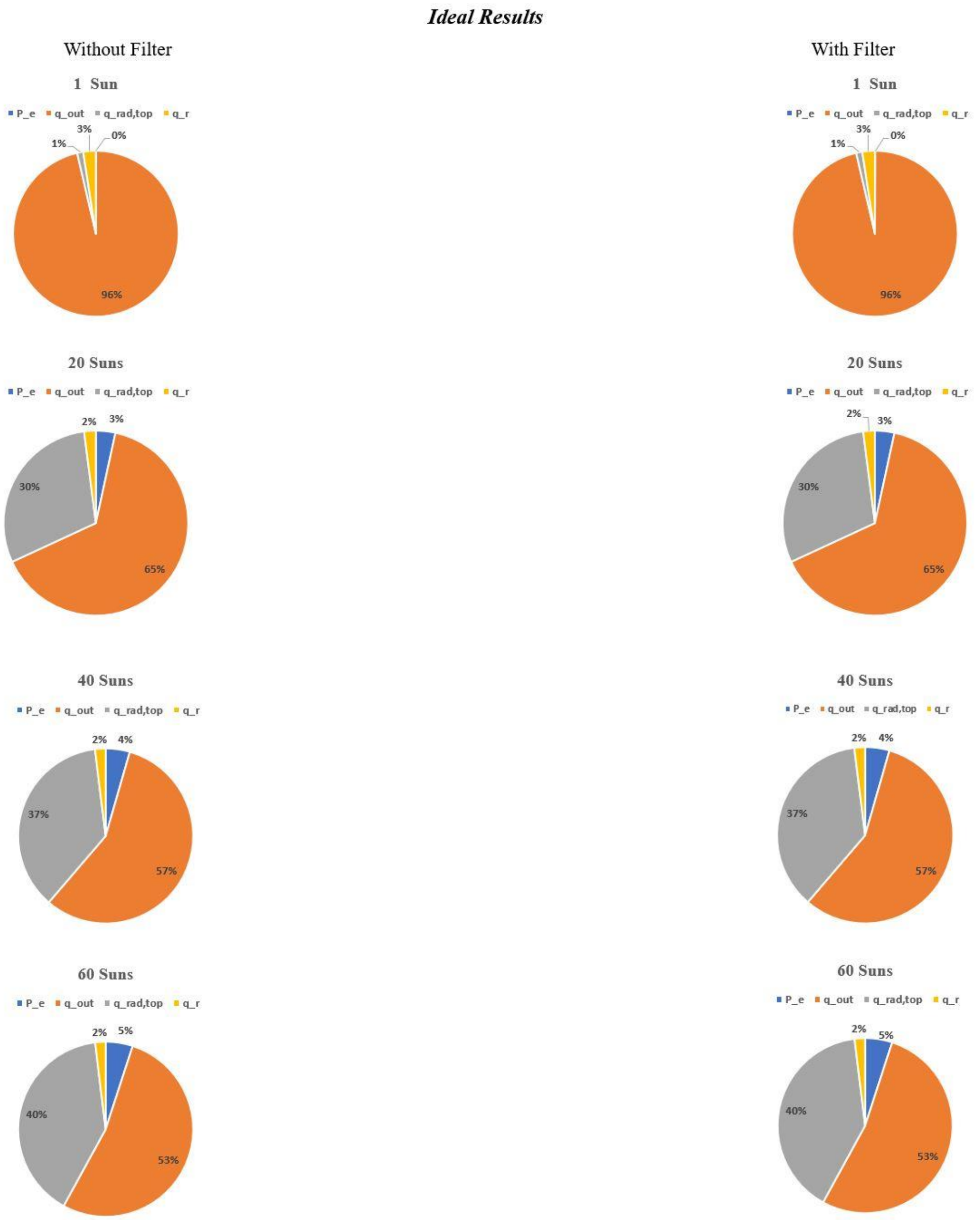

Figure 2.13: Energy pie-chart for ideal absorber

Fig. 2.15 shows the comparison in STPV efficiency for black, ideal, and metafilm absorber. For both metafilm and black absorber, there is a significant increment in STPV efficiency due to the increase in electrical power produced from the PV cell and reduction in emission losses from absorber's surface.

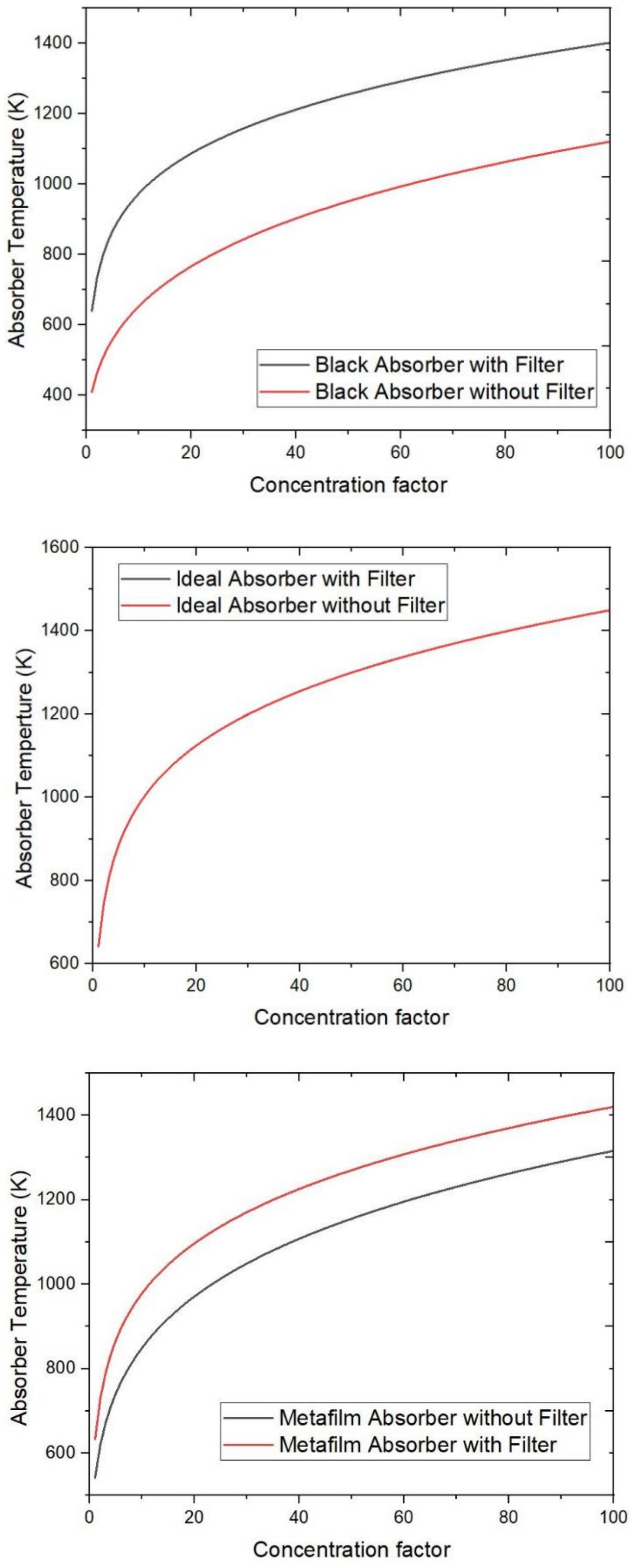

Figure 2.14: Absorber temperature for (top) black (middle) ideal (bottom) metafilm absorber, with and without filter and GaSb cell as the receiver

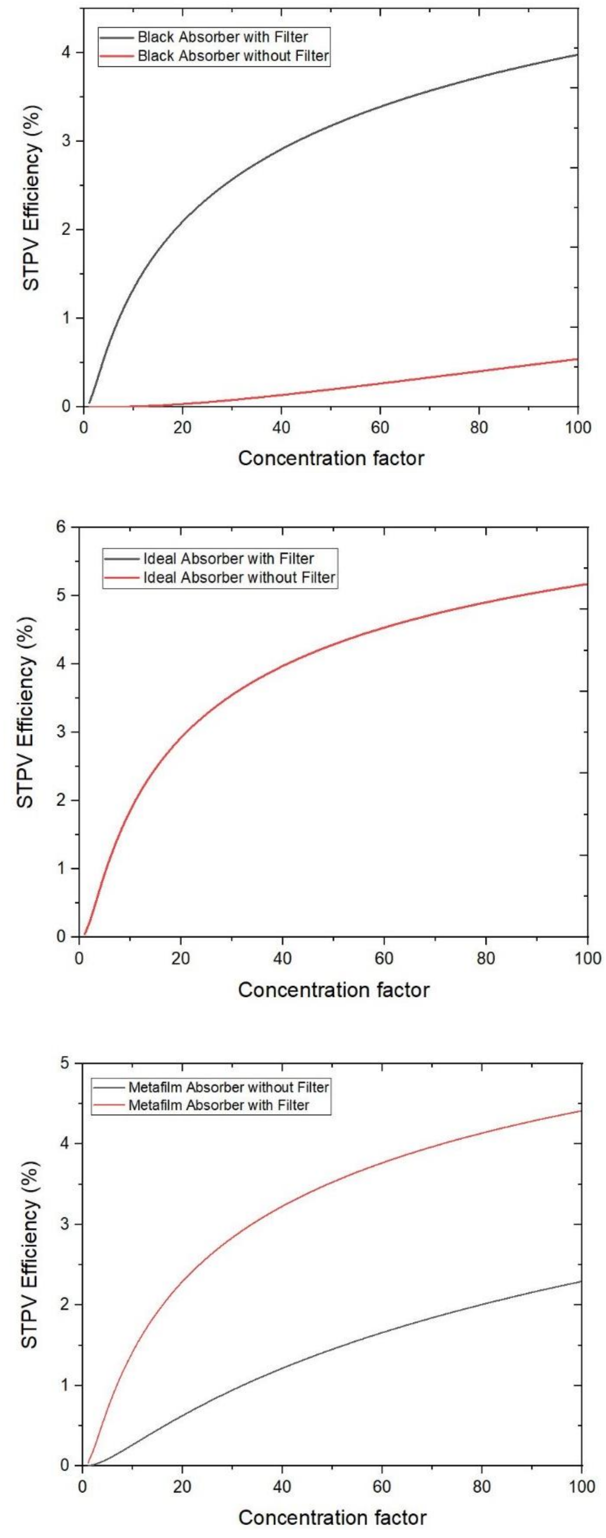

Figure 2.15: STPV Efficiency for (top) black (middle) ideal (bottom) metafilm absorber, with and without filter and GaSb cell as the receiver

CHAPTER 3

EXPERIMENTAL METHODS AND RESULTS

3.1 Experimental Setup and Major Components

A schematic of the experimental setup is shown in Fig. 3.1. The solar irradiation from the Xenon Arc lamp, (Newport, 450-1000 W, F/12) is transmitted through neutral density filters (Thorlabs) for adjusting the concentration factor. Air Mass-1.5 Filter (Thorlabs, AM 1.5 Global) was used to better match the total (direct and diffuse) solar spectrum. A focusing lens (Thorlabs, f = 150 mm) is used to focus the light entering the vacuum chamber on the Ag mirror. The light is then reflected from the Ag mirror and passes through a focusing lens (Thorlabs, f = 75 mm) and Iris on to the Absorber surface. Here, the combination of focusing lens (Thorlabs, f = 75 mm) and Iris is used to concentrate the irradiance precisely on to the absorber surface. The Xe lamp is connected to a DC power supply (Newport, OPS-A1000) to power the lamp with a constant voltage and current. Prolong use of filters degrade during operation their optical properties hence, a fan is used to cool the neutral density filters and the Air-Mass 1.5 filter.

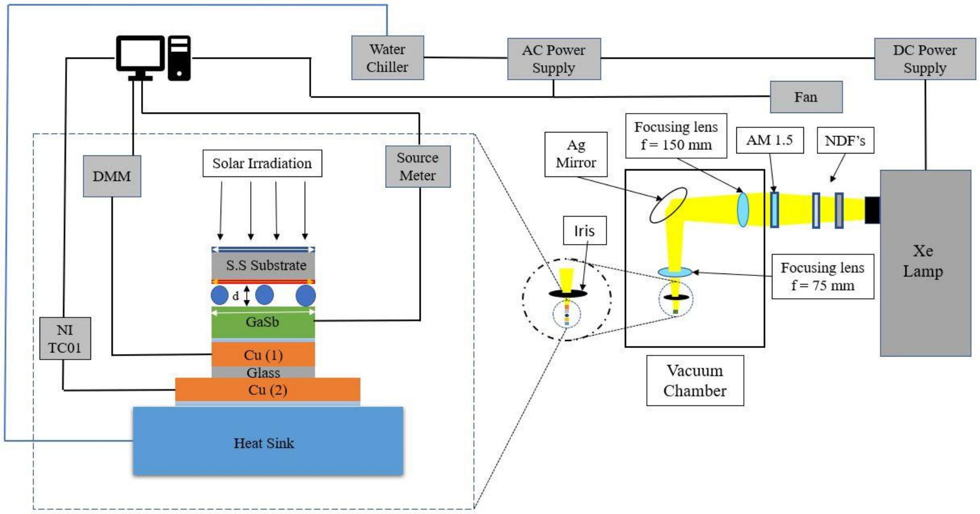

Figure 3.1: Schematic of the Experimental setup

The absorber and emitter metafilm were deposited on a Stainless-Steel substrate of 1 sq.cm. The substrate was first sputtered with Tungsten to reduce its emissivity and thus the side losses. This absorber-emitter module is placed on the top of the GaSb TPV cell at a gap of 100 µm. SiO_2 particles of 100 µm diameter were used to create this gap. Five of these particles were placed on the TPV cell surface, one in each corner and one at the center. To measure the heat flux through the cell, a stack of Cu-Glass-Cu was implanted beneath the cell using a thermal pad. And the same was used to prepare the Cu-Glass-Cu stack.

The Cu piece beneath the receiver was of 1sq.cm with the glass piece of the same size. A 1 sq.in Cu piece was used as the final layer of the stack. Both the Cu pieces were attached with K-type Thermocouples. The thermocouple attached to the 1st Cu piece as shown in Fig. 3.1 is connected to a Digital Multi-Meter (Keithley, DMM-2110). It's used to record the temperature readings and monitor the cell temperature as the 1st Cu piece is directly beneath the TPV cell. Whereas, the 2nd Cu piece temperature is just monitored using a Temperature Sensor (National Instruments, USB-TC01). The cell output i.e. output power density was measured using a Source Metre (Keithley, SMU-2410). The TPV cell temperature is maintained around 300 K to prevent loss in power. A water-cooled heat sink was used to prevent the cell from overheating. Industrial chiller (CW-3000) of 8 Litres capacity was used to circulate the cooling water through the heat sink. The heat sink was tested for leakage before installing it in the actual experimental setup. The leakage tests were implemented in 3 stages and Fig. 3.2 shows the 3rd stage of the leakage test inside the vacuum chamber. Firstly, the copper water block was tested for leakage, then the fluid feedthrough connecting the water block and chiller was tested, and finally, the whole assembly of the heat sink was tested for leakage inside the vacuum chamber. No leakage was found in any of the stages of testing.

As shown in Figs. 3.3,4,5 and 3.6 the entire setup is placed inside a vacuum chamber with several feedthrough ports and a vacuum pump (Pfeiffer HiCUBE) which can reduce the chamber pressure down to 10^{-5} hPa. It takes approximately 1hour to reach this pressure, after which the lamp is turned on and the readings are taken.

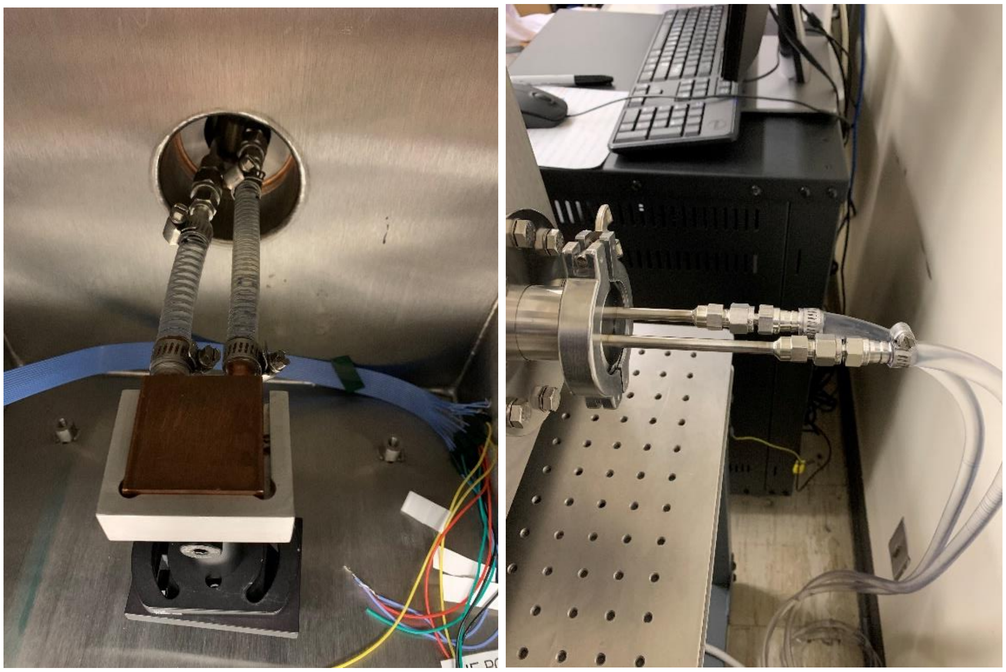

Figure 3.2: Leakage Tests Inside the vacuum chamber

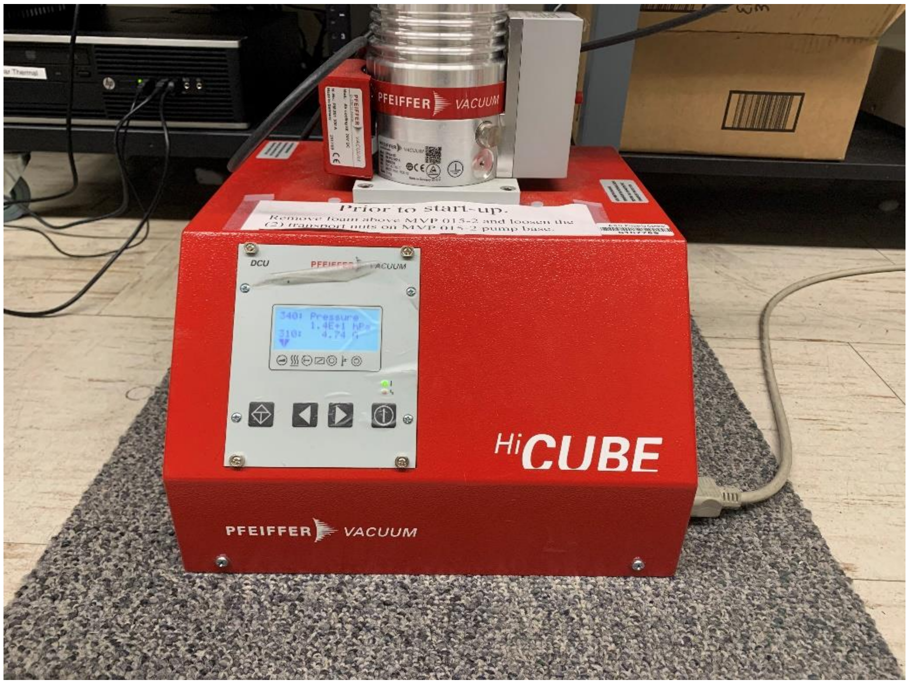

Figure 3.2: Vacuum Pump

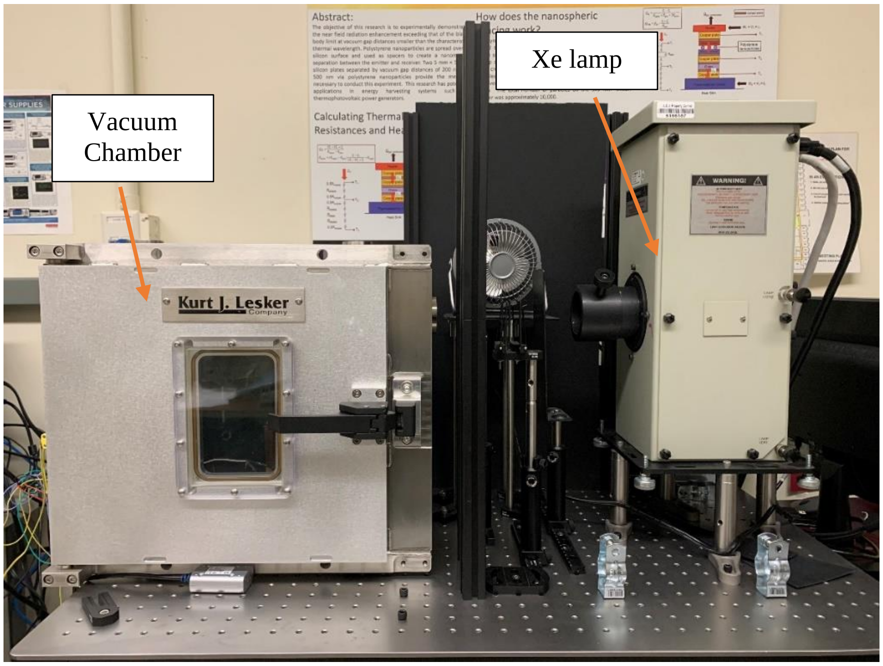

Figure 3.3: Vacuum Chamber

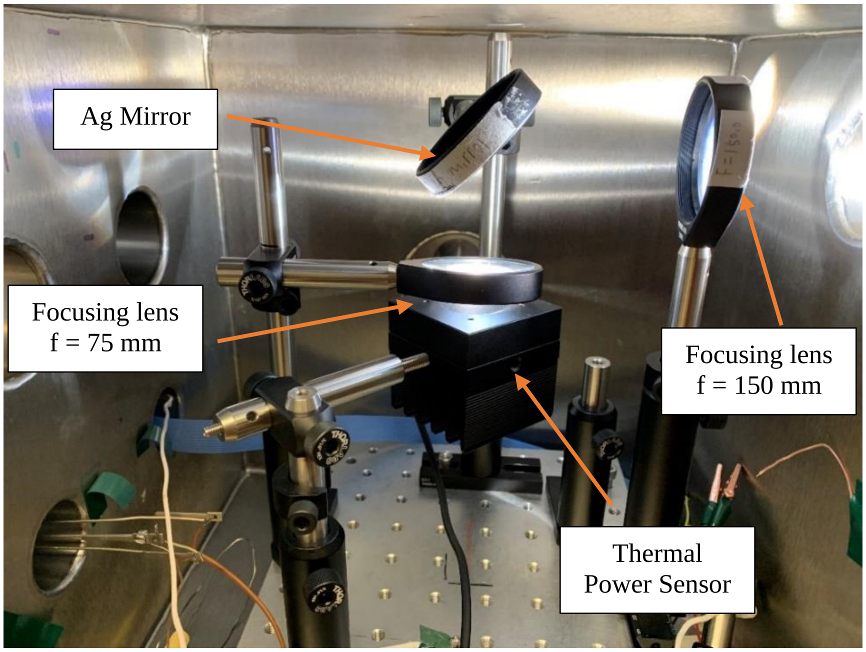

Figure 3.4: Experimental setup picturing focusing lens, Ag mirror and Thermal Power Sensor

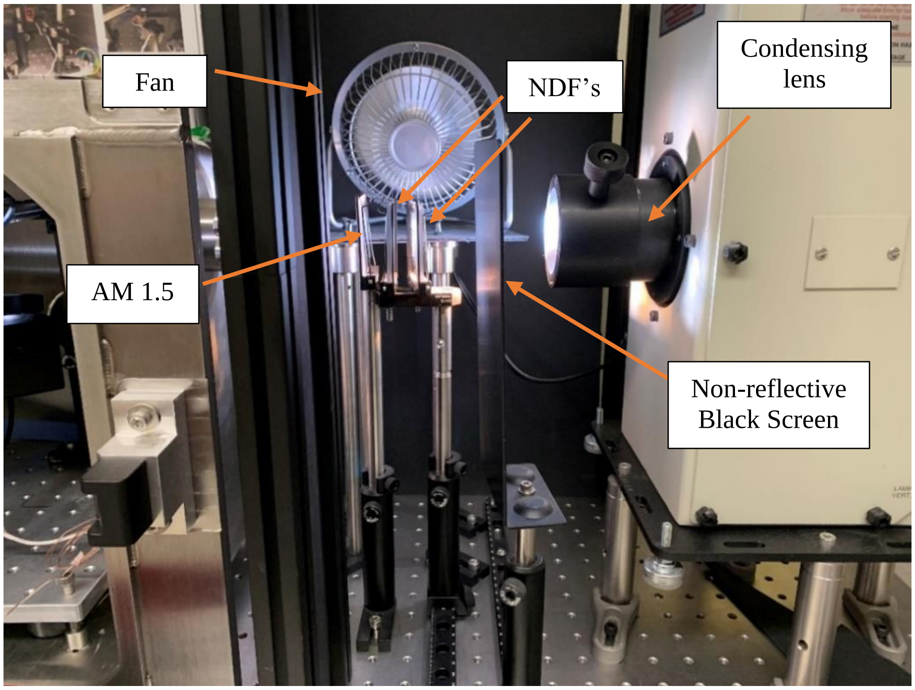

Figure 3.5: Experimental setup picturing NDF's and AM 1.5 Filter

All the required procedures to determine the STPV system efficiency are depicted in the following flow chart.

Adjust the focusing lens inside the vacuum chamber such that maximum power is transmitted to the Absorber

SiO_2 microspheres are placed over the receiver using the needle probe. Then the stack of receiver and Cu piece is placed over the water black inside vacuum chamber.

Absorber-Emitter module is placed over the receiver with glass microsphere and K-type thermocouples are attached to the Cu pieces to record the temperature of the

Vacuum pump is switched on and the pressure inside the vacuum chamber is decreased to 10 ^ (-5) hPa

Solar simulator (Xe Arc lamp) is turned on with the non-reflective screen in front of the condensing lens till the power stabilizes

Water chiller is turned on to keep the receiver temperature around room temperature during the experiment

Neutral Density Filters (NDF's) are placed in front of the lamp according to the filter combinations and absorber is irradiated with light from the lamp

The output of the receiver is recorded using the Source meter whereas the temperature of the receiver is recorded via DMM

This process is repeated for all the Neutral Density filter combinations

The input power is recorded using the thermal power sensor which is placed beneath the iris in place of the whole setup

⬇

System efficiency is determined from the output of the receiver and power input from lamp for each filter combination

3.2 Measurement of Incident Solar Irradiance at different Concentrations

The solar irradiance from the solar simulator i.e. Xenon Arc lamp, (Newport, 450-1000 W, F/12) is measured using the Thermal Power sensor head (Thorlabs, S310C) which is connected to an optical power and energy meter (Thorlabs, PM100D). The thermal power sensor is placed directly under the Iris, in the position of the test setup as shown in Fig. 3.7, such that the light passing through the iris aperture falls directly on the sensor’s surface. The aperture size was set such that light spot is about right onto the edges of the absorber, the same aperture size was kept for this measurement.

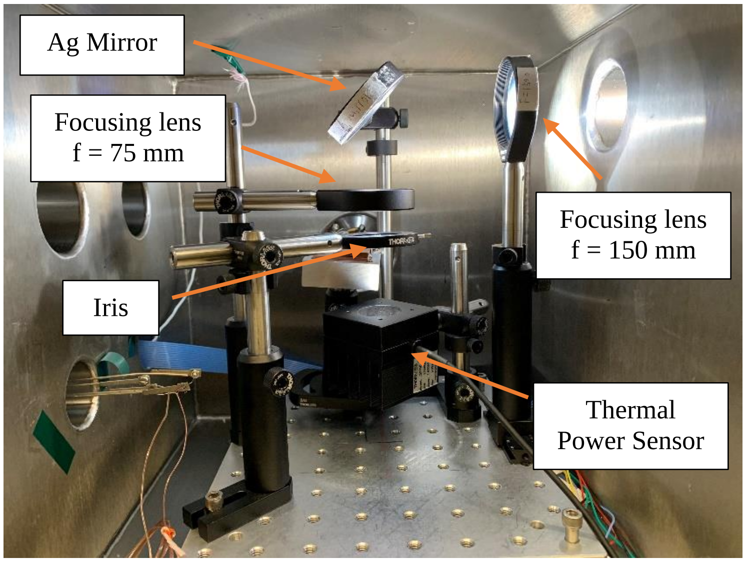

Figure 3.6: Solar Irradiance Measurement setup

Before switching on the lamp for power measurement, the DC power supply (Newport, OPS-A1000) which is used to power the lamp is turned on for approximately 7 minutes along with the fan as shown in Fig. 3.6. The fan is also turned on which is used to cool the NDF's and AM1.5 filter during the operation. After this, the lamp is switched on and the flat non-reflective vertical black screen is kept in front of the lamp for approximately 10 minutes so that the lamp power stabilizes to the power set value, which is 870 W – 907 W in our case. Fig 3.8 shows the arrangement of NDF's and AM 1.5 filter. The properties of NDF's (Thorlabs) used in the experiment are provided in table 3.1.

Figure 3.8: Schematic for the arrangement of NDF's and AM 1.5 filter

Five different combinations of NDF's of different combined transmittance were used to attain different concentration factors and are listed in table 3.2. For each filter combination, three readings are recorded each at a 1-minute interval, from the power sensor. The average of the three readings was taken as the incidence power for a1 filter combination.

Optical Density (OD)	Transmittance (%)	NDF Model Number
1.0	10	FSQ-ND10
0.6	25.1	FSQ-ND06
0.3	50.1	FSQ-ND03
0.1	79.4	FSQ-ND01

Table 3.1: Neutral Density Filter's Properties

The flat non-reflective vertical black screen shown in Fig. 3.6 is used to block the light from the Xenon lamp while changing the filters.

Combination No.	Filter 2 (%)	Filter 1 (%)	Combined Transmittance (%)
1	10	25.1	2.51
2	10	100	10
3	25.1	79.4	19.93
4	50.1	79.4	39.78
5	100	100	100

Table 3.2: Neutral Density Filter combinations

3.3 Fabrication and Optical Properties of Selective Metafilm Absorber/Emitter

The selective multilayer solar absorber/emitter which is made of five layers (i.e. SiO_2-Si_3N_4-W-SiO_2-W from top to bottom) was theoretically, designed fabricated and optically characterized. The top thin layers of SiO_2 and Si_3N_4 serve as anti-reflection coatings in the visible region and thereby increase absorption, whereas the W-SiO_2-W stack at the bottom enhances the absorption at its resonance wavelength within the near-IR region due to the formation of Fabry-Perot cavity [28]. Tungsten was selected due to its high melting temperature which makes it suitable for the high-temperature absorber. The multi-layer absorber/emitter thickness was optimized using particle swarm optimization (PSO) method [29] to achieve the best performance of the selective metafilm absorber/emitter.

The solar absorber optimized at T = 400°C was selected for sample fabrication and characterization. Key parameters such as deposition rate, chamber pressure, and temperature, the layer thickness is listed in the tables below. For better quality, the top thin layers of SiO_2 and Si_3N_4 layers were deposited using chemical vapor deposition (Oxford PECVD), as these layers serve as oxygen passivation layers at the top while heating in air. For the metafilm absorber, the entire multilayer stack has a thickness of around 300 nm, whereas for the emitter the stack thickness is around 500 nm. This multilayer absorber/emitter has zero transmission as the bottom tungsten layer is optically opaque. The key parameters and deposition methods for absorber and emitter metafilm are listed in tables 3.3 and 3.4 respectively.

Material	Deposition Method	Layer thickness (nm)	Deposition rate (Å/s)	Base Pressure (10^{-6} torr)	Chamber Temperature (°C)	Sputtering or RF power (W)
SiO_2 top layer	PECVD	29	~11.67	-	300	-
Si_3N_4	PECVD	41	~4.83	-	300	-
W thin layer	RF Sputtering	9	0.4	2	-	35
SiO_2 cavity	DC sputtering	24	0.65	2	-	200
W substrate	DC sputtering	200	1.2	2	-	100

Table 3.3: Deposition method and parameters for different layers in the multilayer selective solar absorber

Material	Deposition Method	Layer thickness (nm)	Deposition rate (Å/s)	Base Pressure (10^{-6} torr)	Chamber Temperature (°C)	Sputtering or RF power (W)
SiO_2 top layer	PECVD	91	~11.67	-	300	-
Si_3N_4	PECVD	100	~4.83	-	300	-
W thin layer	RF Sputtering	12	0.4	2	-	35
SiO_2 cavity	DC sputtering	100	0.65	2	-	200
W substrate	DC sputtering	200	1.2	2	-	100

Table 3.4: Deposition method and parameters for different layers in the multilayer selective solar emitter

Figs. 3.9 plots the spectrally normal absorptance of the optimized absorber and fabricated absorber metafilm. It can see seen that the metafilm shows good spectral selectivity, i.e. high absorptance from 0.4 to 0.6 µm and low absorptance above 1.6 µm.

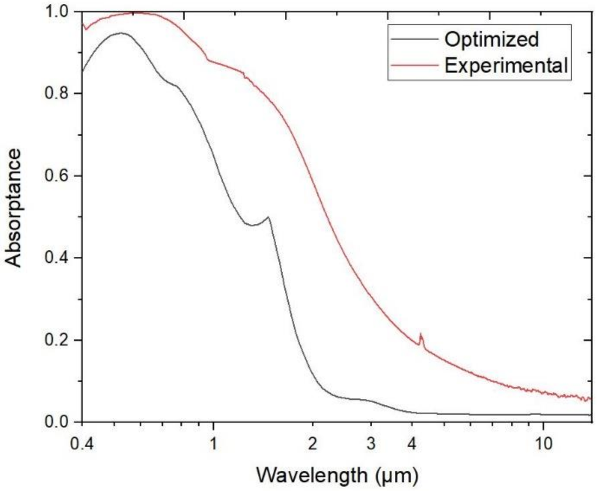

Figure 3.9: Spectral normal absorptance of optimized and fabricated absorber metafilm

Fig. 3.10 plots the emittance of the fabricated selective multilayer solar emitter and the optimized emitter. From Figs. 3.9 and 3.10 we can see that the experimentally measured values are in good agreement with the predicted values for both absorber and emitter metafilm. The fabricated metafilm is of better quality than its optimization.

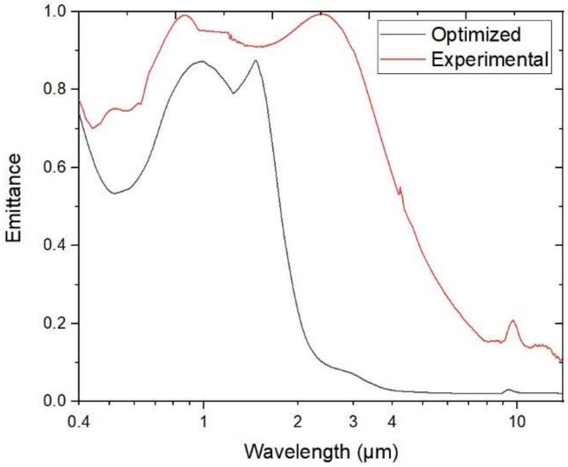

Figure 3.10: Spectral normal emittance of optimized and fabricated emitter metafilm

3.4 Optical and Electrical Properties of GaSb Cells

The GaSb cell from JX Crystals will be used in this experiment and is a Dual Bus Cells type of PV cell with evaporated silver metal on its front and back. The key parameters of the GaSb cell are listed in Table 3.5.

GaSb Substrate	0.65 mm thick
Grid Width	0.0163 mm
Grid Spacing	0.102 mm
Active Area	1.02 cm^2
Ohmic bar width	0.75 mm

Table 3.5: GaSb Cell parameters

Fig. 3.11,12 shows the GaSb and its optical image showing the grid of the PV cell, respectively.

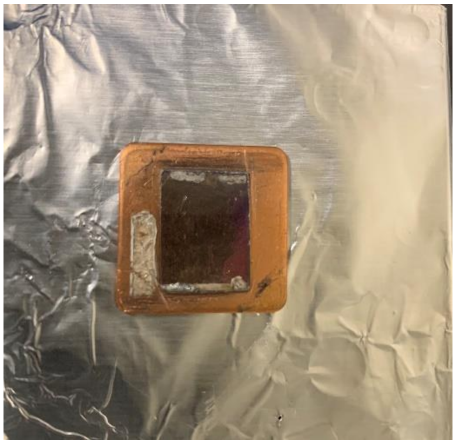

Figure 3.11: GaSb cell

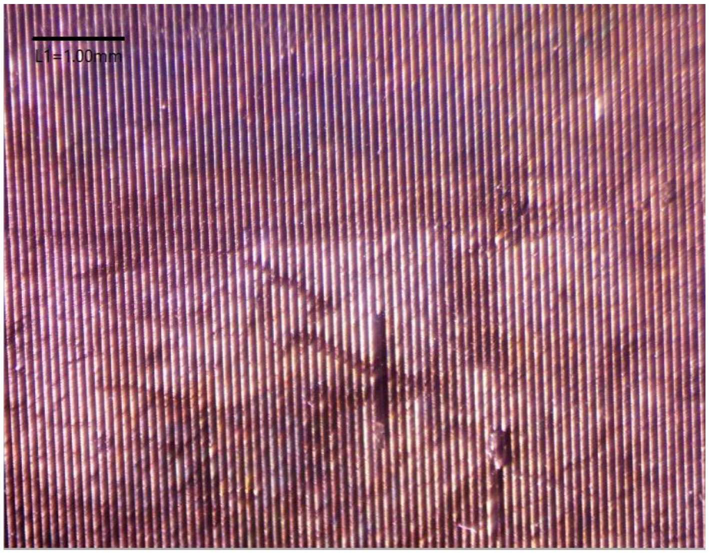

Figure 3.12: Optical Image of the GaSb cell showing grid spacing

To calculate the electrical output power of the TPV cell it's optical and electrical properties i.e. its absorptance and external quantum efficiency (EQE) are needed to be measured. The absorptance is calculated from reflectivity measurements. The reflectance of the GaSb cells is measured using the Integration sphere (Labsphere, RT-060-SF).

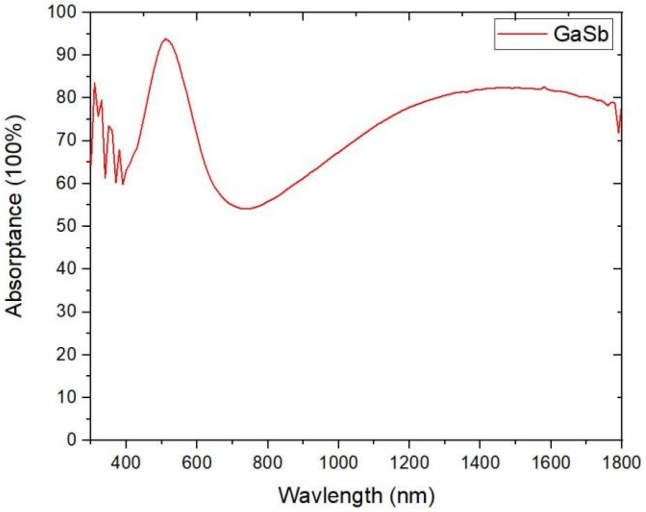

Figure 3.13: Absorptance for GaSb Cell

Fig. 3.13 shows the absorptance of the cell first increases sharply in the visible region but then it reaches its peak near 550 nm and then drops rapidly to around 55% absorptance. The absorptance then increases smoothly and remains constant around 80% in the near-IR region.

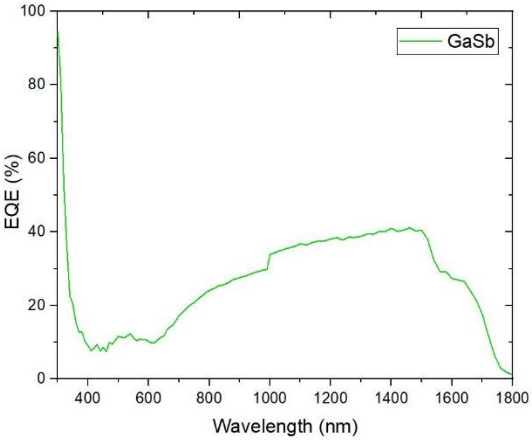

Figure 3.14: EQE efficiency for GaSb cell

The measured EQE of the GaSb cell, sharply decreases in the visible region and increases gradually in the near-IR region and reaches its maximum around 1500 nm wavelength as seen in Fig. 3.14.

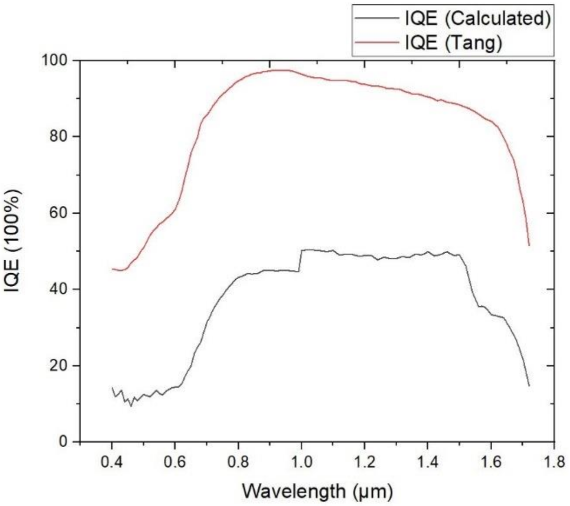

Figure 3.15: IQE for GaSb cell

Fig. 3.15 shows the trend of IQE for the GaSb TPV cell used in the experiment and its efficiency is compared with the IQE of the GaSb cell used by Tang et.al. [30]. From Fig. 3.15 we can see that the GaSb cell has high internal quantum efficiency in the near-IR region but is significantly low as compared to Tang et.al This could be due to degradation of the PV cell over the years of its use, another possible reason is the low external quantum efficiency of the cell used in the experiment.

3.5 Preparation of Glass Microsphere Spacers

The glass microspheres used to create the gap between the absorber-emitter module and TPV cells were placed over the receiver one at a time using a needle-probe under a microscope. A total of 5 particles were placed on the cell, one at each corner and the 5th particle in the center of the cell to create the gap evenly and avoid any contact of the emitter to the receiver. Each particle of 100 mm diameter was captured using a digital microscope.

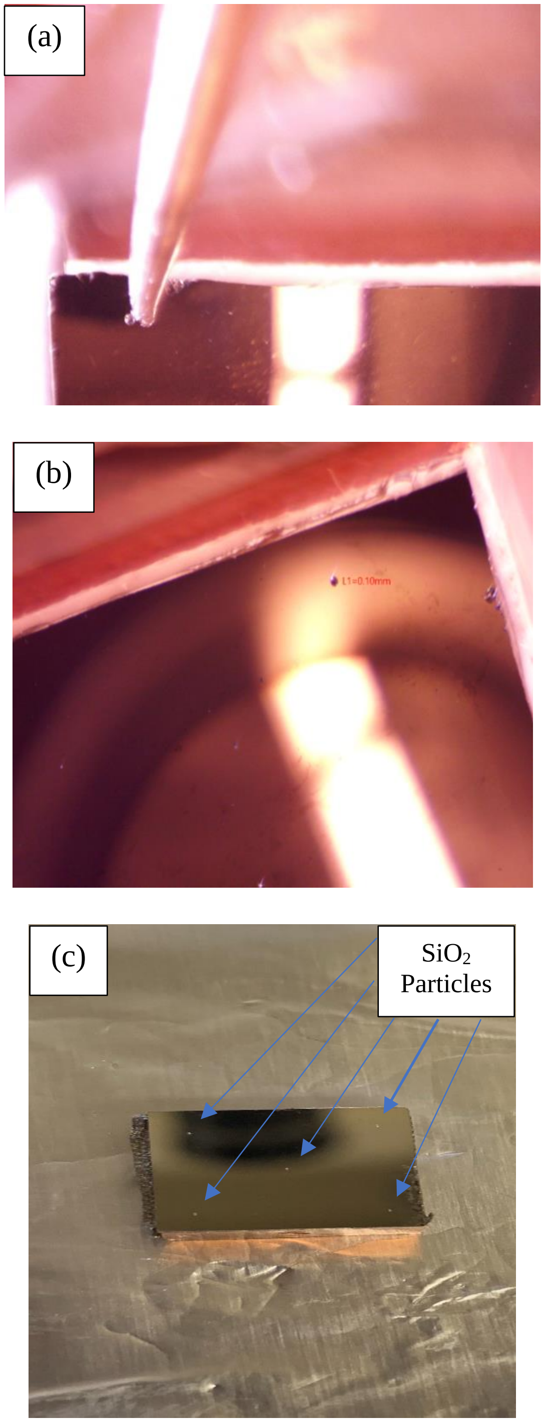

Figure 3.16: (a) Needle used to place SiO_2 particle (b) Calibrated and measured the diameter of a SiO_2 particle and (c) 5 SiO_2 particles placed on Dp-Si

3.6 Temperature and Heat Flux Measurements

The theoretical model developed was validated by performing experiment with Dp-Si as the receiver and fabricated metafilm as absorber and emitter. The absorber-emitter module fabricated in section 3.3 was used to absorb solar irradiance and then emit at the tailored wavelength to the doped-Si. The complete setup for this step can be seen in Fig. 3.17 and 3.18

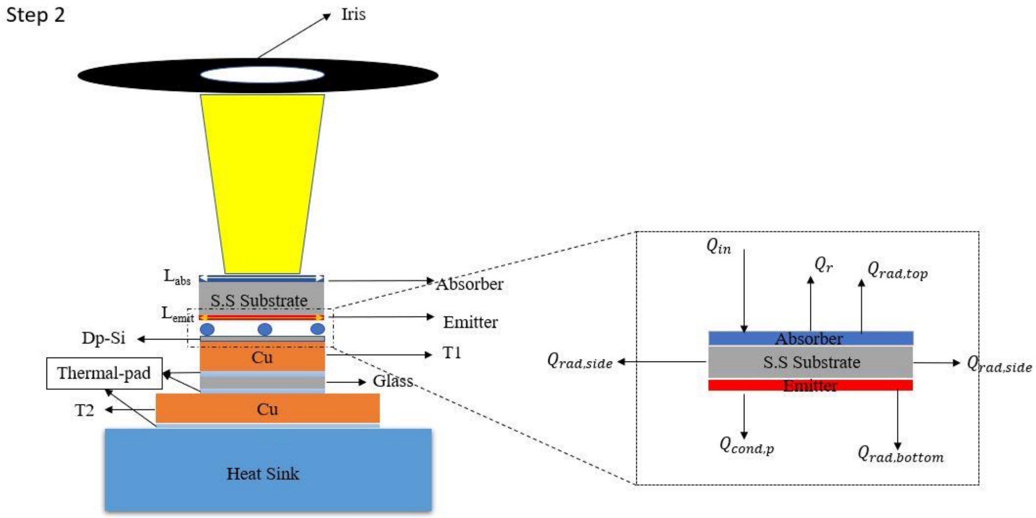

Figure 3.17: Theoretical Model for Heat transfer rate across the glass slide for the experiment.

$$Q_{rad,bottom} = \iint_0^\infty \frac{E_{b\lambda}(T_{emit}) - E_{b\lambda}(T_{Dp-Si})}{\frac{1-\varepsilon_{emit}(\lambda)}{\varepsilon_{emit}(\lambda)} + \frac{1}{F_{emit-Dp\_Si}} + \frac{1-\varepsilon_{Dp\_Si}(\lambda)}{\varepsilon_{Dp\_Si}(\lambda)}} d\lambda dA \quad \textbf{(24)}$$

$$Q_{cond,p} = \frac{T_{emit} - T_1}{R_{Cond}} \quad \textbf{(25)}$$

$$Q_{c,model} = Q_{rad,bottom} + Q_{cond,p} \quad \textbf{(26)}$$

Heat transfer across the glass side of 1.17 mm thickness was calculated experimentally by measuring temperature across the glass slide with 2 copper pieces. Two

K-type thermocouples were used to measure the temperature of the Cu blocks. T_1 thermocouple was connected to DMM (Keithley 2110) for logging the data whereas T_2 was connected to a temperature sensor (NI, USB-TC01). A thermal pad was used to glue Dp-Si, Cu, glass slide together over the water block. The theoretical model used to validate this experiment can be seen in Fig. 3.17 whereas Fig. 3.18 shows the experimental calculation and thermal contact resistance network for the rate of heat transfer across the glass slide. The value of thermal contact resistance for the thermal pad was taken from [31] where they calibrated the contact resistance using a heat flux meter.

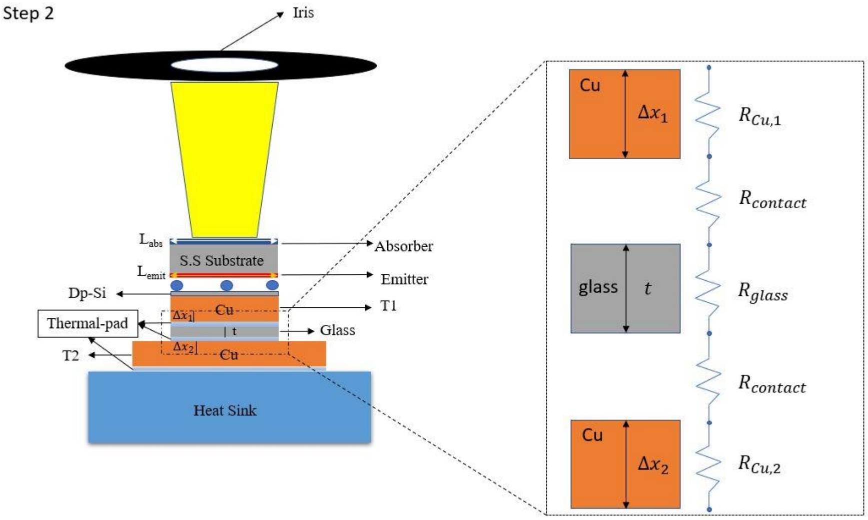

Figure 3.18: Experimentally determined Heat transfer rate across the glass slide in the experiment.

$$R_{Cu,1} = \frac{\Delta x_1}{k_{Cu} A} \quad \textbf{(27)}$$

$$R_{contact} = 0.32\, K/W \quad \textbf{(28)}$$

$$R_{glass} = \frac{t}{k_{glass} A} \quad \textbf{(29)}$$

$$R_{Cu,2} = \frac{\Delta x_2}{k_{Cu} A} \quad \textbf{(30)}$$

$$Q_{c,exp} = \frac{(T_1 - T_2)}{(R_{Cu,1} + R_{contact} + R_{glass} + R_{contact} + R_{Cu,2})} \qquad \textbf{(31)}$$

The experiment was performed in a vacuum pressure of 10^{-5} hPa. This experiment was repeated thrice to verify the results. Fig. 3.19 shows the results of the experiment. The figure shows good repeatability among the data points in the three experiments performed. The accuracy of the two K-type thermocouples used in the experiment was also checked using icy water (0°C) and both showed good accuracy of ±0.5°C.

We can see from the results of the experiment there is good agreement between experimental and theoretical heat transfer rate for approximately all data sets except for the last set where $Q_{c,model}$ is less than $Q_{c,exp}$, this can be seen in Fig. 3.19. The contact resistance is responsible here for the decrement of $Q_{c,model}$ with respect to $Q_{c,exp}$ as the temperature difference increases. The contact resistance data I used in calculating the $Q_{c,exp}$ was taken from a source as mentioned above and not calibrated according to my setup.

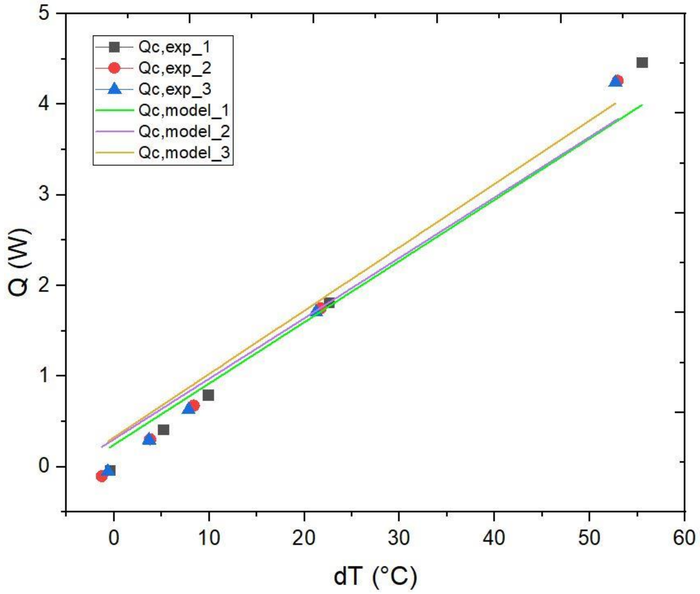

Figure 3.19: Comparison for $Q_{c,exp}$ and $Q_{c,model}$

3.7 Uncertainty Analysis

Also, measurement uncertainty $U_c = k_c\sqrt{(u_A^2 + u_B^2)}$, including both precision (u_A) from three independent experiments for the above mentioned experiments, and accuracy (u_B) from error propagation, was considered for the experimental heat transfer rate across the glass slide. From equation (32) we know

$$Q_{c,exp} = \frac{(T_1 - T_2)}{(R_{Cu,1} + R_{contact} + R_{glass} + R_{contact} + R_{Cu,2})}$$

Assuming, $$B = (T_1 - T_2) \quad \textbf{(32)}$$

And $$C = (R_{Cu,1} + R_{contact} + R_{glass} + R_{contact} + R_{Cu,2}) \quad \textbf{(33)}$$

$$C = \frac{\Delta t_{Cu,1}}{k_{Cu}A} + 0.32 + \frac{\Delta t_{glass}}{k_{glass}A} + 0.32 + \frac{\Delta t_{Cu,2}}{k_{Cu}A} \quad \textbf{(34)}$$

Temperature readings have ±0.05°C uncertainty due to thermocouple accuracy, whereas the length measurements of the glass slide and Cu pieces have an uncertainty of 0.00001 m from the Vernier caliper accuracy. Uncertainty for B can be calculated using adding the uncertainties of both temperature readings in quadrature –

$$\delta B = \sqrt{(0.5^2 + 0.5^2)} \quad \textbf{(35)}$$

For the term, C fractional uncertainties for each term are added in the quadrature.

$$x = \frac{\Delta t_{Cu,1}}{k_{Cu}A} \quad \textbf{(36)}$$

$$y = \frac{\Delta t_{glass}}{k_{glass}A} \quad \textbf{(37)}$$

$$z = \frac{\Delta t_{Cu,2}}{k_{Cu}A} \quad \textbf{(38)}$$

As for the $R_{contact}$ the value was taken from a source, its uncertainty is neglected.

$$A = l \times l, \qquad l = 0.01\,m \quad \textbf{(39)}$$

$$\delta\Delta t_{Cu,1} = \delta\Delta t_{glass} = \delta\Delta t_{Cu,2} = \sqrt{((0.00001)^2 + (0.00001)^2)} \quad \textbf{(40)}$$

$$k_{Cu}l = 385 \times 0.01 = 3.85 \;\&\; k_{glass}l = 1 \times 0.01 \tag{41}$$

And the uncertainty of l is also multiplied by k_{Cu}

Therefore,

$$\frac{\delta(k_{Cu}l \times l)}{k_{Cu}A} = \sqrt{\left(\left(\frac{\delta(k_{Cu}l)}{k_{Cu}l}\right)^2 + \left(\frac{\delta l}{l}\right)^2\right)} \tag{42}$$

Similarly,

$$\frac{\delta\left(k_{glass}l \times l\right)}{k_{glass}A} = \sqrt{\left(\left(\frac{\delta(k_{glass}l)}{k_{glass}l}\right)^2 + \left(\frac{\delta l}{l}\right)^2\right)} \tag{43}$$

Now we can calculate the uncertainties for terms $x, y,$ and z –

$$\frac{\delta x}{x} = \sqrt{\left(\left(\frac{\delta \Delta t_{Cu,1}}{\Delta t_{Cu,1}}\right)^2 + \left(\frac{\delta(k_{Cu}l \times l)}{k_{Cu}A}\right)^2\right)} \tag{44}$$

$$\frac{\delta y}{y} = \sqrt{\left(\left(\frac{\delta \Delta t_{glass}}{\Delta t_{glass}}\right)^2 + \left(\frac{\delta\left(k_{glass}l \times l\right)}{k_{glass}A}\right)^2\right)} \tag{45}$$

$$\frac{\delta z}{z} = \sqrt{\left(\left(\frac{\delta \Delta t_{Cu,2}}{\Delta 2}\right)^2 + \left(\frac{\delta(k_{Cu}l \times l)}{k_{Cu}A}\right)^2\right)} \tag{46}$$

Combining the uncertainties of terms $x, y,$ and z –

$$\delta C = \sqrt{(\delta x)^2 + (\delta y)^2 + (\delta z)^2} \tag{47}$$

Uncertainty in $Q_{c,exp}$ due to propagation of error can be evaluated as

$$\frac{\delta Q_{c,exp}}{Q_{c,exp}} = \sqrt{\left(\frac{\delta B}{B}\right)^2 + \left(\frac{\delta C}{C}\right)^2} \tag{48}$$

Therefore,

$$u_B = \delta Q_{c,exp} = Q_{c,exp} \times \sqrt{\left(\frac{\delta B}{B}\right)^2 + \left(\frac{\delta C}{C}\right)^2} \tag{49}$$

Uncertainty due to precision (u_A) can be calculated by evaluating the Standard Deviation of $Q_{c,exp}$ for the three experiments for each filter combination. Tables 3.5 show the standard deviation for the experiments. The coverage factor k_c is considered as one.

Index	Filter 2	Filter 1	$Q_{c,exp} - 1$	$Q_{c,exp} - 2$	$Q_{c,exp} - 3$	Q_{avg}	$u_A =$ SD	Relative error $u_A(\%)$
1	10%	25.1%	-0.0366	-0.1039	-0.0515	-0.064	0.03532	-55.17
2	10%	100%	0.41535	0.3043	0.29518	0.33827	0.06690	19.78
3	25.1%	79.4%	0.79416	0.67428	0.63024	0.69955	0.08483	12.13
4	50.1%	79.4%	1.81592	1.7482	1.70715	1.7570	0.05492	3.126
5	100%	100%	4.46473	4.25911	4.24076	4.3215	0.12435	2.877

Table 3.5: Standard Deviation of the Experiments

Fig. 3.20 shows the experiment value of heat transfer across the glass slide by red markers with error bars as combined uncertainties U_c.

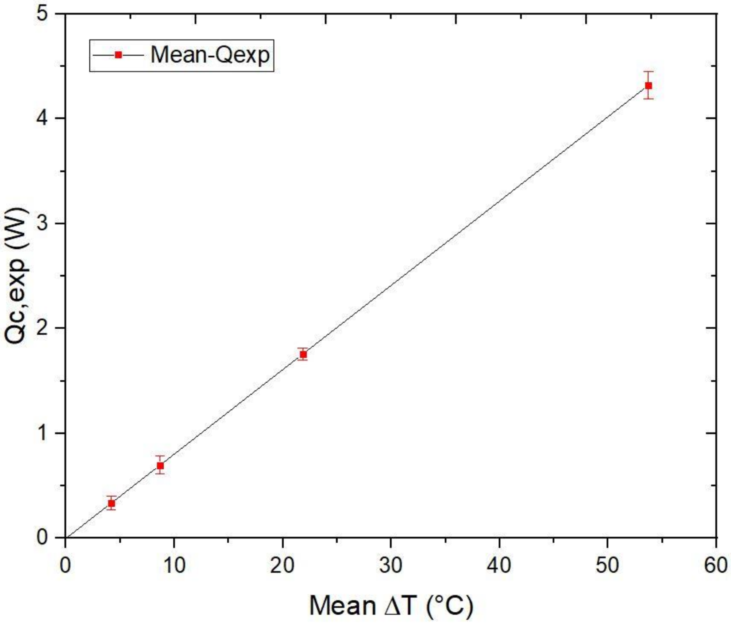

Figure 3.20: Measured $Q_{c,exp}$ with error bars at different ΔT for the Experiments

Here, in Fig. 3.20 the mean value of $Q_{c,exp}$ among the three experimental readings for one filter combination, is plotted against the mean value of ΔT with combined uncertainties in $Q_{c,exp}$ for the experiments.

CHAPTER 4

CONCLUSION AND FUTURE RECOMMENDATIONS

4.1 Conclusion

The setup for creating the gap between the emitter and receiver in the planar STPV system using glass microspheres is complete. The selective absorber/emitter metafilm layers thickness was optimized using particle swarm optimization (PSO) method and fabricated using plasma-enhanced chemical vapor deposition (PECVD) and sputtering techniques. The fabricated selective metafilm optical properties deviated from the theoretically optimized metafilm due to the variation in thickness of layers in the multi-layer metafilm.

A theoretical model was developed for the STPV system with glass microspheres as spacers. A code was developed to solve for the absorber/emitter temperature by solving the energy balance equation in theoretical modeling. Simulations for different receivers (Dp-Si, Black surface, and GaSb cell) with selective metafilm as absorber/emitter illustrate the absorber/emitter temperature, conduction losses via glass microspheres and radiation exchange between the emitter and cell. This energy analysis is also demonstrated using energy pie-chart for the three receivers at different concentration factors. Further, the energy pie-chart for the GaSb cell shows the thermalization losses and electrical power produced with the selective metafilm at different suns.

An ideal selective filter/reflector was proposed to increase the STPV system performance by reducing the emission losses from the absorber’s surface. Energy pie-chart for three different absorbers illustrates the increase in electrical power produced and a decrease in emission losses with a filter as compared to the STPV system without a filter.

Experiments were performed in to validate the theoretical model. The experiment with the absorber-emitter module and Dp-Si as receiver produced results with the good agreement of theoretical and experimental values of heat transfer rate across the glass slide.

Uncertainty Analysis was conducted for the experiments mentioned in section 3.6. This was achieved by taking the precision error and propagation of error into account and combining them to get the uncertainty in the heat transfer across the glass slide.

4.2 Future Work

The thermal contact resistance needs to be calibrated using a heat flux meter (HFM) to validate the theoretical model. After the validation of our model, an experiment for evaluating STPV system efficiency using GaSb cell as the receiver and selective metafilm as absorber-emitter will be performed to match the theoretical results.

REFERENCES

[1] Shockley, W., and Queisser, H. J., 1961, "Detailed Balance Limit of Efficiency of P-n Junction Solar Cells," J. Appl. Phys., **32**(3), pp. 510–519.

[2] Wang, Y., Liu, H., and Zhu, J., 2019, "Solar Thermophotovoltaics: Progress, Challenges, and Opportunities," APL Mater., **7**(8).

[3] Buddhiraju, S., Santhanam, P., and Fan, S., 2018, "Thermodynamic Limits of Energy Harvesting from Outgoing Thermal Radiation," Proc. Natl. Acad. Sci. U. S. A., **115**(16), pp. E3609–E3615.

[4] Datas, A., and Algora, C., 2010, "Detailed Balance Analysis of Solar Thermophotovoltaic Systems Made up of Single Junction Photovoltaic Cells and Broadband Thermal Emitters," Sol. Energy Mater. Sol. Cells, **94**(12), pp. 2137–2147.

[5] Zhao, B., Hu, M., Ao, X., Xuan, Q., and Pei, G., 2020, "Spectrally Selective Approaches for Passive Cooling of Solar Cells: A Review," Appl. Energy, **262**(January), p. 114548.

[6] Rinnerbauer, V., Ndao, S., Yeng, Y. X., Chan, W. R., Senkevich, J. J., Joannopoulos, J. D., Soljačić, M., and Celanovic, I., 2012, "Recent Developments in High-Temperature Photonic Crystals for Energy Conversion," Energy Environ. Sci., **5**(10), pp. 8815–8823.

[7] Cao, F., McEnaney, K., Chen, G., and Ren, Z., 2014, "A Review of Cermet-Based Spectrally Selective Solar Absorbers," Energy Environ. Sci., **7**(5), pp. 1615–1627.

[8] Moon, J., Lu, D., VanSaders, B., Kim, T. K., Kong, S. D., Jin, S., Chen, R., and Liu, Z., 2014, "High-Performance Multi-Scaled Nanostructured Spectrally Selective Coating for Concentrating Solar Power," Nano Energy, **8**, pp. 238–246.

[9] Wang, Y., Zhou, L., Zheng, Q., Lu, H., Gan, Q., Yu, Z., and Zhu, J., 2017, "Spectrally Selective Solar Absorber with Sharp and Temperature-Dependent Cut-off Based on Semiconductor Nanowire Arrays," Appl. Phys. Lett., **110**(20).

[10] Lenert, A., Bierman, D. M., Nam, Y., Chan, W. R., Celanović, I., Soljačić, M., and Wang, E. N., 2014, "A Nanophotonic Solar Thermophotovoltaic Device," Nat. Nanotechnol., **9**(2), pp. 126–130.

[11] "Metallic Photonic Crystal Absorber-Emitter for Efficient Spectral Control in High-Temperature Solar Thermophotovoltaics.Pdf."

[12] Machrafi, H., 2012, *Green Energy, and Technology*.

[13] Lenert, A., Nam, Y., Bierman, D. M., and Wang, E. N., 2014, "Role of Spectral

Non-Idealities in the Design of Solar Thermophotovoltaics," Opt. Express, **22**(S6), p. A1604.

[14] Bierman, D. M., Lenert, A., Chan, W. R., Bhatia, B., Celanović, I., Soljačić, M., and Wang, E. N., 2016, "Enhanced Photovoltaic Energy Conversion Using Thermally Based Spectral Shaping," Nat. Energy, **1**(6).

[15] Barshilia, H. C., 2014, "Growth, Characterization and Performance Evaluation of Ti/AlTiN/AlTiON/ AlTiO High Temperature Spectrally Selective Coatings for Solar Thermal Power Applications," Sol. Energy Mater. Sol. Cells, **130**, pp. 322–330.

[16] Nuru, Z. Y., Arendse, C. J., Muller, T. F., Khamlich, S., and Maaza, M., 2014, "Thermal Stability of Electron Beam Evaporated AlxO y/Pt/AlxOy Multilayer Solar Absorber Coatings," Sol. Energy Mater. Sol. Cells, **120**(PART B), pp. 473–480.

[17] Sakakibara, R., Stelmakh, V., Chan, W. R., Ghebrebrhan, M., Joannopoulos, J. D., Soljačić, M., and Čelanović, I., 2019, "Practical Emitters for Thermophotovoltaics: A Review," J. Photonics Energy, **9**(03), p. 1.

[18] Shimizu, M., Kohiyama, A., and Yugami, H., 2015, "High-Efficiency Solar-Thermophotovoltaic System Equipped with a Monolithic Planar Selective Absorber/Emitter," J. Photonics Energy, **5**(1), p. 053099.

[19] Ferguson, L. G., and Fraas, L. M., 1995, "Theoretical Study of GaSb PV Cells Efficiency as a Function of Temperature," Sol. Energy Mater. Sol. Cells, **39**(1), pp. 11–18.

[20] Mauk, M. G., and Andreev, V. M., 2003, "GaSb-Related Materials for TPV Cells," Semicond. Sci. Technol., **18**(5).

[21] Borrego, J. M., Brown, E., Greiff, P., Huffaker, D. L., Laghumavarapu, R. B., Kim, J., and Dutta, P. S., 2014, "Rear Illumination Monolithically Integrated GaSb Thermophotovoltaic Devices Grown on Semi-Insulating GaAs Substrate," J. Renew. Sustain. Energy, **6**(1).

[22] Wilt, D. M., Fatemi, N. S., Jenkins, P. P., Hoffman, R. W., Landis, G. A., and Jain, R. K., 1996, "Monolithically Interconnected InGaAs TPV Module Development," Conf. Rec. IEEE Photovolt. Spec. Conf., pp. 43–48.

[23] Tan, M., Lu, S., Ji, L., Zhu, Y., and Chen, Z., 2013, "Optimization of In0.68Ga0.32As Thermophotovoltaic Device Grown on Compositionally Nonmonotonically Graded InAsP Buffer by Metal-Organic Chemical Vapor Deposition," Jpn. J. Appl. Phys., **52**(11 PART 1).

[24] Tan, M., Ji, L., Wu, Y., Dai, P., Wang, Q., Li, K., Yu, T., Yu, Y., Lu, S., and

Yang, H., 2014, "Investigation of InGaAs Thermophotovoltaic Cells under Blackbody Radiation," Appl. Phys. Express, **7**(9), pp. 18–21.

[25] "Low-Bandgap Ge and InAsSbP-InAs-Based TPV Cells."

[26] Rephaeli, E., and Fan, S., 2009, "Absorber and Emitter for Solar Thermo-Photovoltaic Systems to Achieve Efficiency Exceeding the Shockley-Queisser Limit," Opt. Express, **17**(17), p. 15145.

[27] Soffer, B. H., and Lynch, D. K., 1999, "Some Paradoxes, Errors, and Resolutions Concerning the Spectral Optimization of Human Vision," Am. J. Phys., **67**(11), pp. 946–953.

[28] Wang, L. P., Basu, S., and Zhang, Z. M., 2012, "Direct Measurement of Thermal Emission from a Fabry-Perot Cavity Resonator," J. Heat Transfer, **134**(7), pp. 1–9.

[29] Robinson, J., and Rahmat-Samii, Y., 2004, "Particle Swarm Optimization in Electromagnetics," IEEE Trans. Antennas Propag., **52**(2), pp. 397–407.

[30] Tang, L., Xu, C., Liu, Z., Lu, Q., Marshall, A., and Krier, A., 2017, "Suppression of the Surface 'Dead Region' for Fabrication of GaInAsSb Thermophotovoltaic Cells," Sol. Energy Mater. Sol. Cells, **163(**November 2016), pp. 263–269.

[31] Ying, X., Sabbaghi, P., Sluder, N., and Wang, L., 2020, "Super-Planckian Radiative Heat Transfer between Macroscale Surfaces with Vacuum Gaps down to 190 Nm Directly Created by SU-8 Posts and Characterized by Capacitance Method," ACS Photonics, **7**(1), pp. 190–196.

[32] Park, K., Basu, S., King, W. P., and Zhang, Z. M., 2008, "Performance Analysis of Near-Field Thermophotovoltaic Devices Considering Absorption Distribution," J. Quant. Spectrosc. Radiat. Transf., **109**(2), pp. 305–316.

[33] Ni, Q., Alshehri, H., and Wang, L., 2018, "Highly Efficient Sub-100-Nm Thermophotovoltaic Cells Enhanced by Spectrally Selective Two-Dimensional Metasurface," J. Photonics Energy, **9**(03), p. 1.

[34] Ni, Q., Ye, H., Shu, Y., and Lin, Q., 2016, "A Theoretical Discussion on the Internal Quantum Efficiencies of the Epitaxial Single Crystal GaSb Thin Film Cells with Different P-n Junctions," Sol. Energy Mater. Sol. Cells, **149**, pp. 88–96.